# Hyperspectral Mapping for the Detection of SARS-CoV-2 Using Nanomolecular Probes with Yoctomole Sensitivity

Maha Alafeef, Parikshit Moitra, Ketan Dighe, and Dipanjan Pan*

Cite This: https://doi.org/10.1021/acsnano.1c05226

Read Online

ACCESS | Metrics & More | Article Recommendations | Supporting Information

**ABSTRACT:** Efficient monitoring of SARS-CoV-2 outbreak requires the use of a sensitive and rapid diagnostic test. Although SARS-CoV-2 RNA can be detected by RT-qPCR, the molecular-level quantification of the viral load is still challenging, time-consuming, and labor-intensive. Here, we report an ultrasensitive hyperspectral sensor (HyperSENSE) based on hafnium nanoparticles (HfNPs) for specific detection of COVID-19 causative virus, SARS-CoV-2. Density functional theoretical calculations reveal that HfNPs exhibit higher changes in their absorption wavelength and light scattering when bound to their target SARS-CoV-2 RNA sequence relative to the gold nanoparticles. The assay has a turnaround time of a few seconds and has a limit of detection in the yoctomolar range, which is 1 000 000-fold times higher than the currently available COVID-



19 tests. We demonstrated in ~100 COVID-19 clinical samples that the assay is highly sensitive and has a specificity of 100%. We also show that HyperSENSE can rapidly detect other viruses such as influenza A H1N1. The outstanding sensitivity indicates the potential of the current biosensor in detecting the prevailing presymptomatic and asymptomatic COVID-19 cases. Thus, integrating hyperspectral imaging with nanomaterials establishes a diagnostic platform for ultrasensitive detection of COVID-19 that can potentially be applied to any emerging infectious pathogen.

**KEYWORDS:** hyperspectral imaging, SARS-CoV-2, antisense oligonucleotides, hafnium, dark-field microscopy
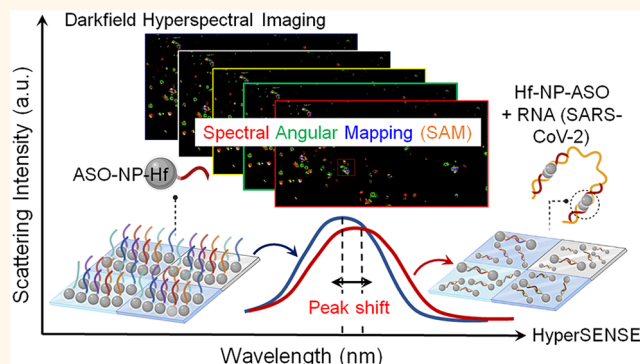
Early identification of infectious diseases is critical in alleviating the transmission of disease by increasing self-isolation and timely care. When COVID-19 exploded onto the global stage in December 2019, public health authorities first deployed measures that were used to control severe acute respiratory syndrome (SARS) in 2003, including symptom-based case identification and eventual isolation and quarantine monitoring.[1−3] This preliminary strategy was justified by several correlations between SARS-CoV and COVID-19 causative virus SARS-CoV-2, including strong genetic correlation, transmission mainly by respiratory droplets, and the occurrence of lower respiratory symptoms including fever, cough, and shortness of breath of both infections emerging within 5 days of exposure.[1,4] However, amid the deployment of identical control measures, the trajectories of the two epidemics have shifted drastically in different directions. To date, SARS-CoV-2 has infected millions of people in one year and continues to spread rapidly across the world.[5] One of the other reasons for the virulent spread of COVID-19 is its closeness with the influenza virus

regarding its clinical presentation, transmission mechanism, and seasonal coincidence.[6] Since both are respiratory viruses, they can have a variety of overlapping symptoms. While certain symptoms are slightly more connected with one virus than the other, a clinical decision cannot be made based on the symptoms to rule in or out either illness. A biosensor is therefore urgently required to selectively detect and distinguish COVID-19 and influenza viruses.

The crucial factor in the rapid transmission of COVID-19 is the high level of SARS-CoV-2 shedding in the upper respiratory tract, even among both asymptomatic and presymptomatic patients.[7,8] For example, SARS-CoV-2 viral

A

**Table 1. Selected ASO Sequences Targeted for the N-Gene of SARS-CoV-2 and HA Gene of Influenza A H1N1 Virus**

| target gene | target sequence (5′−3′) | antisense oligonucleotide sequence (5′−3′) |
| --- | --- | --- |
| N gene of SARS-CoV-2 | ACACCAAAAGAUCACAUUGG | CCAATGTGATCTTTTGGTGT (**ASO1**) |
|  | CCCGCAAUCCUGCUAACAAU | ATTGTTAGCAGGATTGCGGG (**ASO2**) |
| HA gene of influenza A H1N1 | CUAGUACUGUGUCUACAGUGUC | GACACTGTAGACACAGTACTAG (**ASO3**) |
|  | ACAGGAAGCAAAGCACAGGG | CCCTGTGCTTTGCTTCCTGT (**ASO4**) |

load (VL) peaks at 0.7 day before the onset of symptoms, indicating that transmission occurs early in the process of infection.[9,10] Additionally, the VL kinetics in mild and severe cases of COVID-19 as well as VL between asymptomatic carriers and symptomatic COVID-19 patients have no reported differences.[11,12] The World Health Organization (WHO) reports that about 16% of individuals with COVID-19 are asymptomatic and can spread coronavirus, although other statistics suggest that 40% of SARS-CoV-2 transmission is attributed to carriers with no signs of the disease.[13] In contrast, people with asymptomatic cases of influenza typically have lower quantitative VL of secretions from the upper respiratory tract than from the lower respiratory tract and a shorter length of viral secretion than those with symptoms.[14−16] Therefore, the asymptomatic transmission of SARS-CoV-2 is the Achilles' heel of the currently deployed public health strategies to mitigate this pandemic, and hence an ultrasensitive SARS-CoV-2 biosensor is an immediate requirement for the classification among asymptomatic, presymptomatic, and symptomatic COVID-19 patients.[1,17]

Currently, most screening techniques require sampling of body fluids such as nasal fluid, saliva, or blood, followed by nucleic acid-based testing to identify active infections or blood-based serological identification of past infections. Although they are highly sensitive, nucleic acid-based diagnostics may require samples gathered several days postexposure for unambiguous positive detection.[18] For example, in most individuals with symptomatic COVID-19 infection, the most used and reliable test for diagnosis of COVID-19 has been the reverse transcription-polymerase chain reaction (RT-PCR) test, where the SARS-CoV-2 viral RNA in the nasopharyngeal swab as measured by the cycle threshold (Ct) becomes detectable as early as day 1 of symptoms and peaks within the first week of symptom onset.[18] Moreover, a "positive" PCR outcome indicates only the identification of viral RNA and does not generally mean that a viable virus is present.[18] This could potentially lead to missed asymptomatic cases. Therefore, the ability to perform practical real-time COVID-19 screening is extremely crucial in assessing the risk and monitoring pathogen presence in the community.

Toward this end, we developed a universal platform for pathogen detection. We have utilized herein a hyperspectral-based nanoimaging technique (HyperSENSE) for rapid multiplex detection and to distinguish between SARS-CoV-2 and influenza viruses. Hyperspectral imaging is a technique that has gained a lot of attention in the past decade from both the academic and industrial world due to its capability of providing spatial and physicochemical information on the investigated species.[19−23] The hyperspectral microscopes can capture images that contain one full spectrum of the reflected light in each pixel of the image, identifying the spectral response of the nanoparticles and confirming their presence and the way they interact with biological samples. In this study, we used hyperspectral imaging in combination with microscopy to examine the unique scattering signature spectra of molecularly targeted nanoprobes. We hypothesized that the spectra attained from nanoprobes will be highly specific for the metals used for derivation of the nanoparticles and can be potentially used to indicate hybridization or binding events. Due to the differences in sample scattering, it will be also feasible to differentiate the nanoprobes when individual pixels are selected in an area of interest from pixels where the probes will be interacting with the viral nucleic acid.

A class of nanomaterial, hafnium nanoparticles (HfNPs) conjugated to antisense oligonucleotide (ASO), has been employed herein for sensing purposes. The performance of HfNPs has also been compared with similar ASO-conjugated gold nanoparticles. The shift in hyperspectral scattering has also been adequately explained from density functional theoretical calculations. In this work, a hyperspectral imaging technique based on the scattering of light was used for the estimation of the viral RNA concentration. The goal of this study was to propose a hyperspectral imaging-based technique for biosensing. To the best of our knowledge, this is an unexplored area, and our study established here that a reflectance scattering-based system can successfully be used for detecting a very low level of viral nucleic acid in biological samples. Here we introduce a hyperspectral imaging-based platform that can be used to diagnose a multitude of diseases. The potential for the development of a point of care (POC)-type device can easily be envisioned; however this was out of the scope of the current work. Overall, the currently developed technique, because of its extremely low detection limit, has the potential to differentiate and discriminate among presymptomatic, asymptomatic, and symptomatic positive COVID-19 patients from the negative ones.

## RESULTS AND DISCUSSION

**Design of Antisense Oligonucleotides for Targeting Pathogen's RNA.** To selectively target the pathogen's RNA, we have chosen to design antisense oligonucleotides. These ASOs are single-stranded DNA (ssDNA) sequences that can specifically recognize and bind to their target complementary RNA strands. We designed a pair of ASOs that is highly specific and sensitive to SARS-CoV-2 N-gene (Supplementary Data 1).[17,23] The methodology behind the design of ASOs has been mentioned in the Materials and Methods section. Briefly, the target binding energies and binding disruption energies were carefully compared to select the ASO sequences specific for the SARS-CoV-2 N-gene. Further, to initiate nanoparticle aggregation in the presence of the target RNA, only the ASOs targeting closely following regions in their target sequence were selected. Separately, to expand the applicability of the current HyperSENSE system for the multiplex detection of SARS-CoV-2 and influenza, we have also utilized two ASOs,[24,25] which target the hemagglutinin (HA) gene of influenza A H1N1 virus. Table 1 shows the ASO sequences specific for SARS-CoV-2 or influenza A H1N1 which have been used throughout this study.
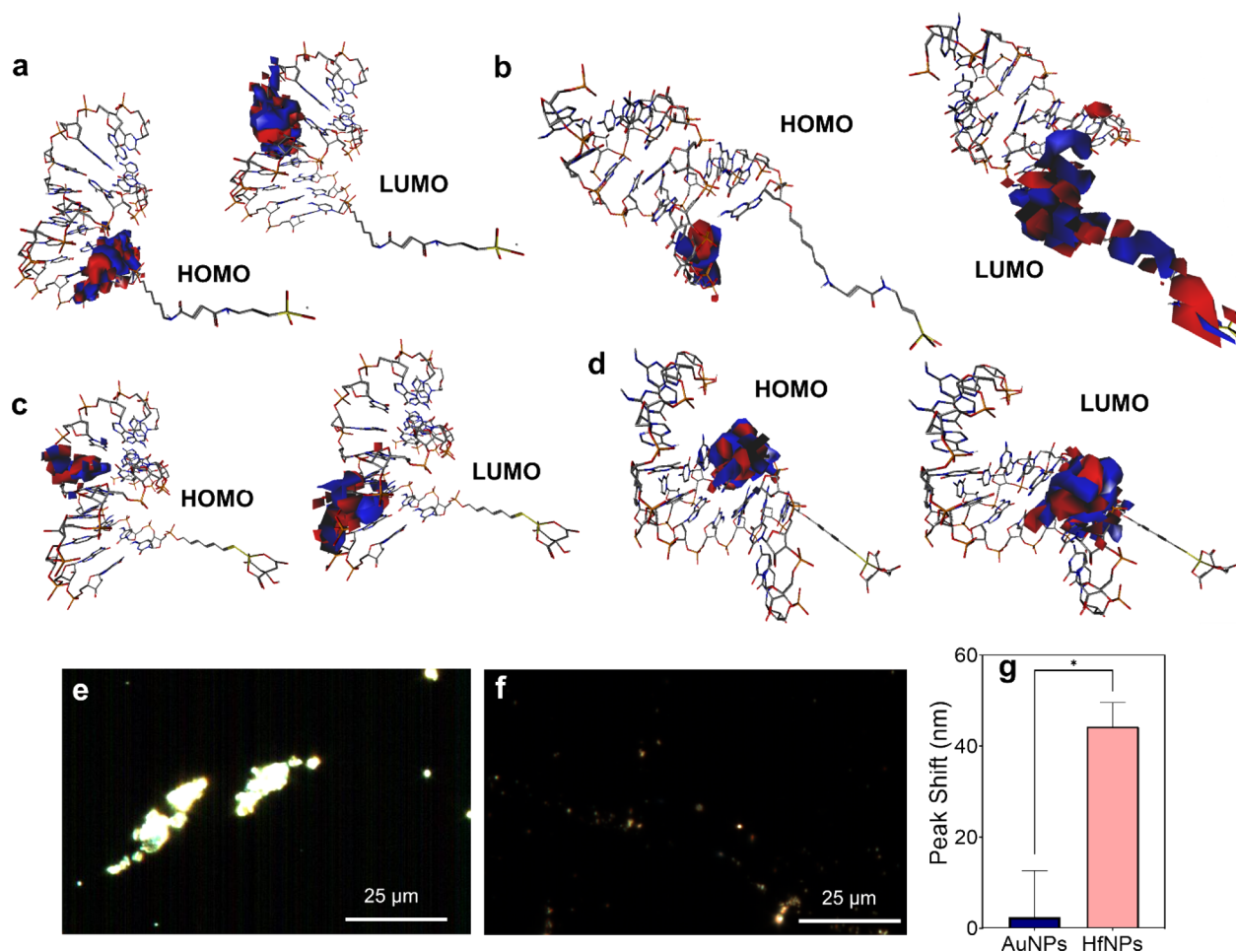
**Figure 1.** Selection of nanoparticle probe for HyperSENSE platform construction. Pictorial diagram of HOMO and LUMO for (a, c) ASO1- and (b, d) ASO2-conjugated (a, b) Hf and (c, d) Au nanoparticles while bonded in their docked geometry with the target SARS-CoV-2 RNA sequence. Enhanced dark-field hyperspectral imaging (EDF-HSI) for (e) HfNPs-P$_{mix}$, and (f) AuNPs-P$_{mix}$, respectively, after the addition of SARS-CoV-2 RNA. (g) Shift in the hyperspectral signal as obtained from the AuNPs and HfNPs as a sensing probe ($n = 3$, $P < 0.05$).

**Design, Synthesis, and Validation of Hyperspectral-Responsive Nanoprobes for the Selective Detection of Viral RNA.** Hyperspectral-based imaging techniques possess the ability to capture spectral information for multiple wavelengths at each pixel in an image.[23,26,27] This capability offers the ability to discriminate, with precision, different nanomaterials and differentiate them from biological materials.[28,29] Nanoparticles are an excellent candidate for sensor construction due to their photophysical properties.[23,30] Our current sensor platform relies on one such important parameter, in which the aggregation among nanoparticles will induce a change in their light scattering. Hyperspectral imaging (HSI) is capable of identifying individual nanoparticles in pure suspensions and in the presence of biological samples by their intrinsic scattering spectra without the use of any additional labeling agent. The technique therefore will be ideal for detecting metallic nanoparticles with unique spectral scattering signatures and achieve highly sensitive nondestructive molecular detection. In this study, we investigated two types of nanoparticles for constructing the biosensor. Hafnium nanoparticles and gold nanoparticles (AuNPs) were synthesized to test their sensing performance. While AuNPs are widely used for biomedical and biosensing applications,[17,23,31−33] HfNPs remained unexplored, especially for sensing purposes.

Density functional theoretical calculations were judiciously employed first to investigate the differential interaction of two ASOs conjugating two types of nanoparticles before and after the hybridization with their target RNA sequence. Initially, the target RNA sequences, ASO1- and ASO2-conjugated HfNPs and AuNPs, were energy minimized. The sequences considered for theoretical calculations are represented in Table S1, and the corresponding energy-minimized structures are shown in Figure S1. The ASO-conjugated nanoparticles were then docked with their target RNA sequences in Autodock 4.0 software, and the respective geometries are shown in Figure S2. It was understood that the ASO1-conjugated nanoparticles stabilized their target RNA sequences better than the ASO2-conjugated nanoparticles plausibly due to improved hydrogen bonding among the participating nucleotides. HfNPs (Figure S3), ASO-conjugated HfNPs (Figure S4), and AuNPs (Figure S5) and the corresponding docked geometries were further considered for the calculation of HOMO and LUMO surface maps, and the energy gaps between them were calculated (Figure 1a−d). From the comparative HOMO−LUMO surface energies, it has been found that the binding of ASO-conjugated nanoparticles with their complementary target RNA sequences leads to a decrease in band gap (Table 2), and hence it has been anticipated that the binding would increase in absorption wavelength (Figure

S6), which might be followed by an increase in hyperspectral scattering.

**Table 2. Comparison Table on the Calculation of the Band Gap between the ASO-Conjugated Gold and Hafnium Nanoparticles with Their Target RNA Docked Geometries**

| name | $\Delta E_{LUMO-HOMO}$ in Hartree | $\Delta E_{LUMO-HOMO}$ in eV |
|---|---|---|
| AuNPs-ASO1 | 0.0016 | 0.044 |
| Au-ASO1-conjugated with target RNA | 0.0009 | 0.024 |
| Au-ASO2 | 0.0044 | 0.12 |
| Au-ASO2-conjugated with target RNA | 0.0031 | 0.084 |
| HfNPs | 0.0667 | 1.815 |
| Hf-ASO1 | 0.0017 | 0.046 |
| Hf-ASO1-conjugated with target RNA | 0.0005 | 0.014 |
| Hf-ASO2 | 0.0033 | 0.09 |
| Hf-ASO2-conjugated with target RNA | 0.0004 | 0.011 |

It was also observed that the comparative band gap was reduced more for HfNPs than for the AuNPs. This indicated an increased change in absorbance and increased light scattering in the case of HfNPs compared with AuNPs. It was also understood that there is close interaction among the target RNA and ASO sequences, leading to the charge transfer primarily from target RNA to the ASO sequence (Figure 1a–d). The theoretical results thus reveal that HfNPs-conjugated ASOs would provide strong light scattering (*i.e.*, better response in the hyperspectral imaging) upon the hybridization with the target RNA when compared to the AuNPs.

To experimentally validate the findings, HfNPs and AuNPs were synthesized[17,23,34] and conjugated with ASOs. The ASOs are amino-modified at the 5′ end in the case of HfNPs, while they are thiol-modified for AuNPs. The surface chemistry of the nanoparticles was suitably altered for the conjugation with ASOs, and the detailed protocol has been described in the Methods and Materials section. The performance of HyperSENSE was first investigated toward the detection of SARS-CoV-2, and for that, each of the HfNPs and AuNPs was conjugated to ASOs specific for SARS-CoV-2. Each particle has been conjugated differentially where AuNPs-$P_1$ and HfNPs-$P_1$ are the nanoparticles conjugated to ASO1 and AuNPs-$P_2$ and HfNPs-$P_2$ are the nanoparticles conjugated to ASO2, respectively. Equal amounts of the AuNPs-$P_1$ and AuNPs-$P_2$ were mixed to form the testing particles, AuNPs-$P_{mix}$. The same was carried out to make a hafnium testing solution, HfNPs-$P_{mix}$. The enhanced dark-field hyperspectral imaging (EDF-HSI) of the HfNPs-$P_{mix}$ (Figure 1e) and AuNPs-$P_{mix}$ (Figure 1f) after the addition of SARS-CoV-2 viral RNA reveals that HfNPs-$P_{mix}$ exhibits higher light scattering when compared to the corresponding AuNP derivative and, thus, better HSI response. Further, we found that HfNPs-$P_{mix}$ outperformed AuNPs-$P_{mix}$ in terms of the peak shift in the hyperspectral signal associated with the addition of the SARS-CoV-2 RNA, as shown in Figure 1g. The significant increase in the shift of the hyperspectral peak of HfNPs-$P_{mix}$ compared to AuNPs-$P_{mix}$, which significantly corroborates with the theoretical findings, motivates us to utilize HfNPs as a sensing probe to construct the sensor platform.

**Methodology of the HSI-Based SARS-CoV-2 Detection Using HyperSENSE.** The strategy adopted for highly sensitive detection of SARS-CoV-2 genetic materials using the HSI chip is depicted in Figure 2. The chip consists of HfNPs conjugated to a selective antisense oligonucleotide (ssDNA probes), which recognizes the target sequence. The hybridization of the ssDNA probes with its complementary sequence causes the aggregation of the HfNPs, which can be detected by HSI. HSI is a sensitive technique that analyzes a wide spectrum of light to obtain information that is not available when imaging with primary colors (red, green, blue). A shift in the HSI peak can be observed due to the aggregation of nanoparticles and the formation of large entities of various sizes. Hyperspectral imaging of the HfNPs conjugated to the ssDNA probes (HfNPs-$P_{mix}$) has been recorded instantaneously upon addition of the test sample in order to obtain the sensor response of the tested sample (Figure 2a). The use of HfNPs serves the purpose of amplifying the HSI signal upon the hybridization of the ssDNA with its target. Next, in order to perform further analysis, the image is divided into numerous regions of interest. The HSI image of any specific spatial location represents a collection of hundreds of images at different wavelengths. Thus, each pixel has hundreds of intensities, which can be seen as a continuous spectrum of light ranging from the visible range to the near-infrared (NIR). The amount of target RNA present in the sample can be determined based on the shift in the hyperspectral peak (Figure 2b). The investigation of the HSI of HfNPs-ssDNA probes may therefore be beneficial in detecting the DNA/RNA hybridization events.

**Construction of Each Component of the HyperSENSE Platform for SARS-CoV-2 Detection.** Once the sensitivity of the HfNP-based probes has been validated, HfNPs were used to construct the sensor platform. First, we evaluated the stability of the HfNPs using the dynamic light scattering (DLS) technique under different conditions. Figure S7 depicts the hydrodynamic diameter of HfNPs in phosphate-buffered saline (PBS), water, and viral transfer media (VTM). In addition to that, the stability of HfNPs was studied at two temperatures, *i.e.*, 25 and 65 °C. As evident from the results, the size of HfNPs did not significantly change among the three mediums. This confirms the stability of the HfNPs in different mediums, where no medium-induced aggregation was observed. Increasing the temperature from 25 °C to 65 °C does not show a significant effect on the size of the HfNPs, confirming the stability of the particles (Figure S8). Based on our observation, the highest contrast in hyperspectral imaging is associated with the highest particle concentration. The concentration of 1 mg/mL was found to be the maximum that can be suspended in the solution without the formation of large aggregates; therefore we utilized this concentration for conducting our sensing studies. HfNPs were prepared and surface modified to have carboxylic acid moieties on the surface for their functionalization with ssDNA probes. ssDNA designed for SARS-CoV-2 detection was then conjugated to surface-modified HfNPs as shown in Figure 2c and Figure S9, where HfNPs-P1 and HfNPs-P2 are the nanoparticles conjugated to ASO1 and ASO2, respectively. NMR spectra indicate the presence of pentose sugar (deoxyribose) protons; this proves the successful conjugation of ASOs with HfNPs (Figure S10). We hypothesized that in the presence of the target sequence the hybridization of the ssDNA probes leads to the aggregation of the HfNPs, which can be detected using
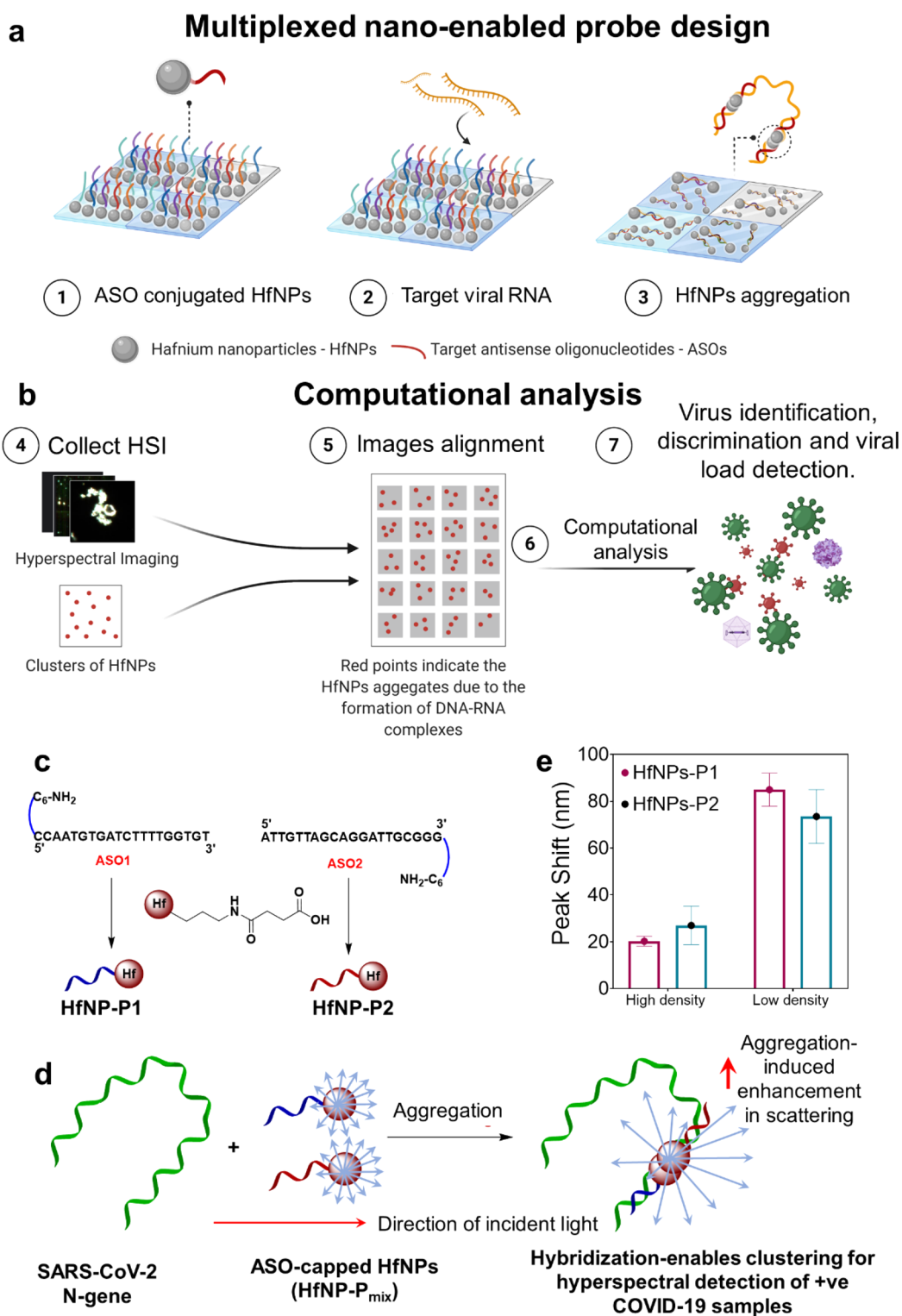
**Figure 2. Schematic diagram on the development of the ultrasensitive SARS-CoV-2 biosensor, HyperSENSE, and the conjugation of ssDNA probes to the HfNPs and the sensing mechanism. (a) The sample is added to the HfNPs-P$_{mix}$. Upon the hybridization of RNA with the ssDNA conjugated to HfNPs, the formation of large entities takes place. This can be detected as a shift in light scattering that can be detected using HSI to identify the presence of COVID-19. (b) The collected HSI will be analyzed by first determining the regions of interest (ROI). The hyperspectral signals will be analyzed to determine the peak wavelength in nm. The shift in the peak of the sample compared to the reference sample (*i.e.*, HfNPs-P$_{mix}$ alone) is calculated and used for virus identification, discrimination, and viral load detection. (c) Conjugation chemistry of the ssDNA probes to the HfNPs. (d) Sensing mechanism of the ssDNA-conjugated HfNPs with the SARS-CoV-2 genetic material. (e) Peak shift as observed by HSI upon the addition of 97.21 fM SARS-CoV-2 viral RNA for the HfNPs with two different ssDNA conjugation ratios.**
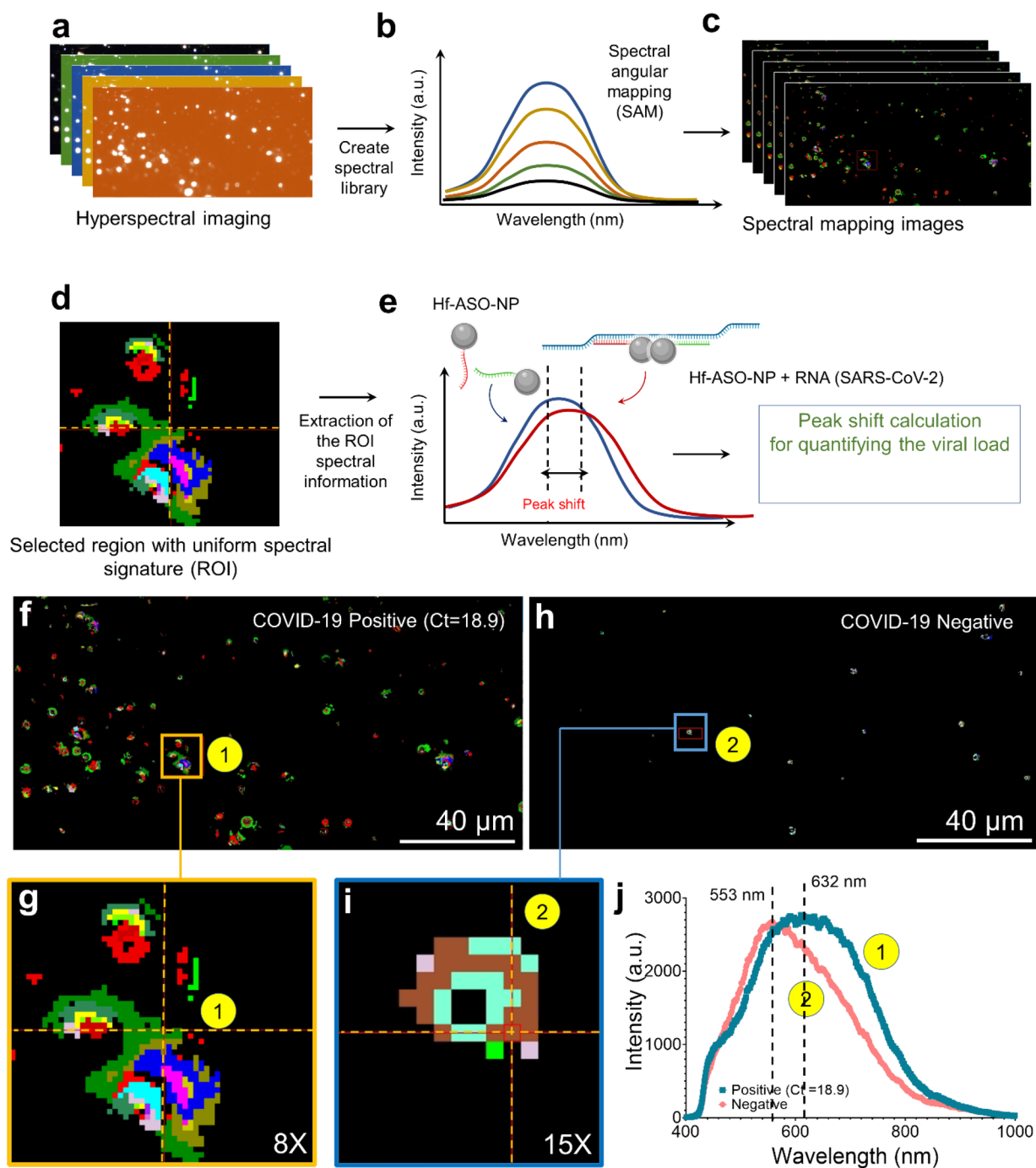
**Figure 3.** Computational analysis of HyperSENSE to find the predominant spectral signature and its workflow. (a) The hyperspectral imaging will be captured of the sample mixed with HfNPs-P$_{mix}$. (b) Region of interest (ROI) including the particle clusters will be used to generate the spectral library. (c) Spectral angular mapping (SAM) algorithm will be used to map the spectral library and define the spectral signature location using a color code. (d) Zoomed-in image of (c) where the spectral signature represented by the green color is predominant in this image. Thus, the ROI (containing the green color) will be used to obtain the HyperSENSE spectral output. (e) The obtained hyperspectral image from the selected region of the predominant color. The peak shift with respect to the HfNPs-P$_{mix}$ spectrum will be used for COVID-19 diagnosis and viral load detection. (f) Hyperspectral mapping image of the spectral component of the image superimposed on the enhanced dark-field image of a COVID-19 positive sample (Ct number = 18.9). (g) Zoomed-in image of mapping in (f). (h) Hyperspectral mapping image of the spectral component of the image superimposed on the enhanced dark-field image of the COVID-19 negative sample. Formation of large clusters can be observed where the spectral signature annotated by the green color is predominant in the COVID-19 sample. (i) Zoomed-in image of (h) where the brown color is predominant in the image. (j) Predominant spectral signature in both positive (green) and negative (brown) samples. The positive sample showed a significant peak shift when compared with the negative sample.

HSI (Figure 2d). The HfNPs/ssDNA ratio plays a significant role in the sensitivity and the sensor response. Thus, to evaluate the effect of the ssDNA concentration on the sensor performance and to find the optimum HfNPs/ssDNA ratio,
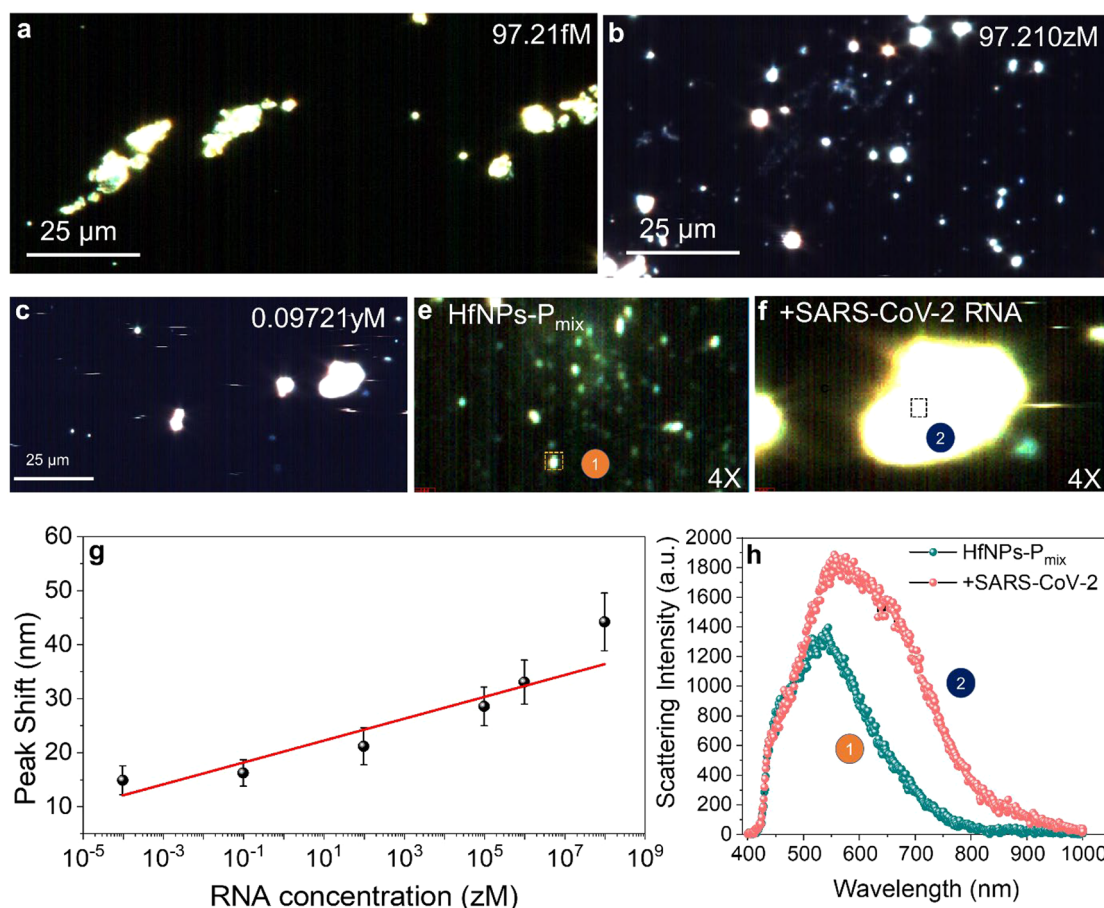
**Figure 4.** Sensitivity of the developed HyperSENSE platform in detecting SARS-CoV-2 presence. EDF-HSI of the ssDNA conjugated to HfNPs (HfNPs-$P_{mix}$) in the presence of SARS-CoV-2 RNA with concentrations of (a) 97.2 fM, (b) 97.21 zM, and (c) 0.09721 yM. The presence of SARS-CoV-2 RNA leads to the aggregation of HfNPs to form large entities. (e) EDF-HSI of the ssDNA conjugated to HfNPs (HfNPs-$P_{mix}$) in the absence of the target and (f) in the presence of SARS-CoV-2 RNA at very low concentration, ~0.1 yM. 4×: amplification of four times of a 100× oil objective. HyperSENSE enables the detection of SARS-CoV-2 RNA at a very low concentration of ~0.1 yM. (g) Standard curve of HyperSENSE, which shows that the SARS-CoV-2 $\log_{10}$(RNA) is linearly proportional to the peak shift; Pearson's correlation = 0.94, $R^2$ = 0.88. (h) Hyperspectral signal of the HfNPs-Pmix in the absence and presence of SARS-CoV-2 RNA (0.09721 yM). A significant shift in the signal peak can be observed after the addition of a sample containing SARS-CoV-2 genetic material. The experiments were performed with experimental repeats of $n$ = 8.

two different concentrations of the ssDNA probes (*i.e.*, ASO1 and ASO2) have been investigated, low-density and high-density probes. Figure 2e depicts the shift in the hyperspectral peak of the two HfNP systems upon the addition of SARS-CoV-2 RNA. Although a high density of ssDNA conjugated to particles means a higher aggregation response, the shift in the HSI peak does not follow the same trend. We found that a low ssDNA probe density exhibits the maximum change in the HSI peak, whereas the particles with a high probe density exhibit the highest scattering intensity. The nanoparticles with a high probe density exhibit a high light scattering in which the signal captured using HSI leads to detector saturation and also exhibited a low change in the hyperspectral peak as a response to the target RNA compared to the low probe density. Thus, we use the HfNPs with a low density of ssDNA probes to construct the sensor array.

**Computational Analysis.** The computational analysis of the captured images involves the following steps as explained in Figure 3a−e. First, a representative spectral library from the collected images was assembled. These images will comprise a collection of the spectra presented in the captured image. Second, the spectral angular mapping (SAM) algorithm was applied to generate the hyperspectral mapping image by assigning each pixel in the image to its reference spectrum. SAM is a powerful algorithm used to determine the spectral similarity between two spectra and match the pixel to the reference spectrum. SAM calculates the angle between the two spectra (*i.e.*, the reference spectrum and the spectrum in a certain pixel) by treating each of them as a vector. The equation for calculating the spectral angle is given by

$$a = \cos^{-1} \frac{\sum_{i=1}^{n} t_i r_i}{\sqrt{\sum_{i=1}^{n} t_i^2} \sqrt{\sum_{i=1}^{n} r_i^2}}$$

where $n$ is the number of bands, $t$ is the pixel spectrum, and $r$ is the reference spectrum. Thus, it compares the angle between the reference spectrum vector and the spectrum vector at each pixel in the image. The closest match to the reference spectrum is associated with the smaller angle, whereas an angle higher than the set threshold represents an unclassified pixel. Each color represents one spectrum, and pixels with the same color have the same spectrum or their spectra are closely matching (Figure S11). Next, the dominant spectrum that has the highest distribution percentage among the image pixels will be
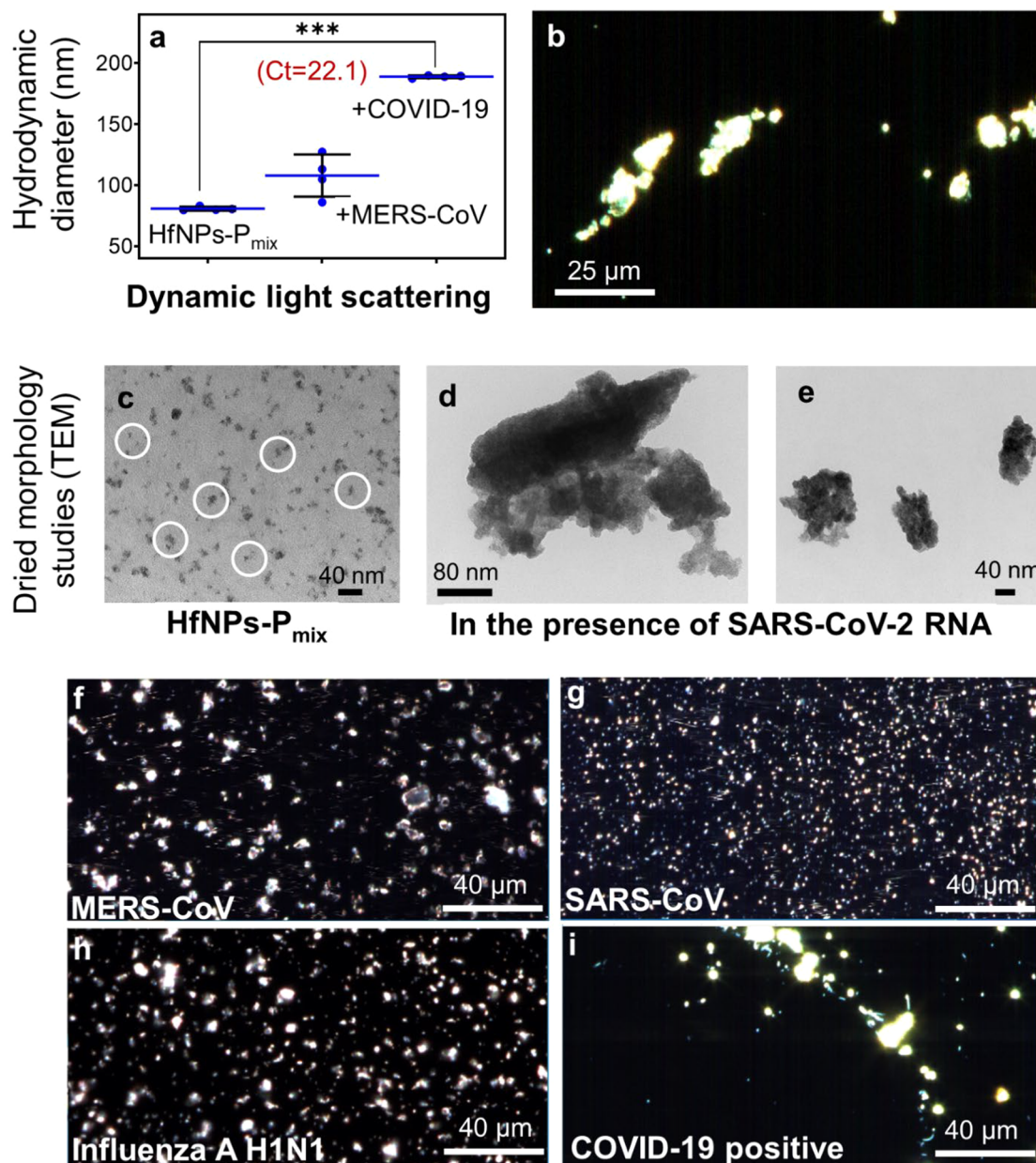
**Figure 5.** Aggregation of the HfNPs is shown using ZetaView, TEM, and EDF-HSI. (a) Hydrodynamic diameters of the HfNPs-$P_{mix}$ in the presence of SARS-CoV-2 and MERS-CoV RNA ($n = 4$, $P < 0.001$). (b) EDF-HSI of the HfNPs-$P_{mix}$ in the presence of SARS-CoV-2 genomic RNA. TEM images of (c) HfNPs-$P_{mix}$ and (d, e) in the presence of SARS-CoV-2 RNA. EDF-HSI of the HfNPs-$P_{mix}$ in the presence of (f) MERS-CoV, (g) SARS-CoV, (h) influenza A H1N1, and (i) SARS-CoV-2 RNA from COVID-19 confirmed clinical samples. The HfNPs-$P_{mix}$ shows a significant aggregation in the presence of SARS-CoV-2 RNA, whereas no obvious formation of large entities was observed as a response to MERS-CoV, SARS-CoV, and influenza A H1N1.

selected. The distribution percentage of each spectrum can be computed by calculating the number of pixels that have the same spectrum divided by the total number of pixels in the image. Finally, the output of the HyperSENSE sensor is calculated by measuring the shift in the peak of the dominant spectrum with respect to the spectrum of HfNPs-$P_{mix}$ alone in the absence of the biological target.

Figure 3f depicts the mapping image of the COVID-19 positive sample confirmed using RT-qPCR (Ct number 18.9). Each color represents one spectrum, and pixels with the same color have the same spectrum or their spectra are closely matching (Figure S11). Figure S11a showed a representative hyperspectral mapping image of the COVID-19 positive

sample. Figure S11b depicts a zoom-in image of the hyperspectral mapping, where each color in the image is labeling each pixel with the reference spectrum that matches its recorded spectrum using the SAM algorithm. The reference spectra used as input for the SAM algorithm are shown in Figure S11c. The color codes are shown in Figure S11d. The variation in the spectrum found in the image during the mapping presumably is attributed to the heterogeneity of formed clusters when bonded to the target RNA. Several clusters with various sizes and nanoparticulate contents may form because the ASOs are covering the surface of the HfNPs, and this may lead to variation in the hyperspectral signal. However, this variation will not affect the sensor sensitivity and

specificity as demonstrated by the functional performance of HyperSENSE with clinical samples. This is attributed to the robust computational workflow used in the data analysis. Our computational algorithm compensates for the limitation that may arise due to the variation in the hyperspectral signals by considering the dominant spectrum and use it for further analysis. It is worth mentioning that the system has 60× and 100× magnification capabilities. The hyperspectral imaging was recorded at a 1.5 nm spectral resolution in the visible to NIR wavelength range from 400 to 1000 nm to allow the detection of minute pixel-to-pixel spectral differences in a hyperspectral image. A quartz halogen aluminum reflector lamp with 75% power was used as illumination source. The hyperspectral image was captured using a CCD camera, and the data were processed using ENVI software. Figure 3h illustrates the mapping of the negative COVID-19 sample using the spectral library collected from the assigned ROI. Figure 3g shows that the spectral signature with a peak at ~632 nm (represented by the green color) is predominant in the HSI of the COVID-19 positive sample. However, the negative sample has a predominant spectral signature with a peak of ~553 nm (represented by brown color) (Figure 3i). The spectral signatures from both positive and negative COVID-19 samples are shown in Figure 3j. These spectra represent the output of the HyperSENSE sensor and can be further used to diagnose COVID-19 and quantify the viral load in the test sample. It is worth mentioning that the saturated pixels were eliminated and were not included during the analysis. This was achieved by excluding the pixels with any saturation or peak clipped signal. Therefore, any pixel that contains a saturated signal will be labeled as an unclassified pixel. The image analysis involved in HyperSENSE was done computationally starting from the spectral library mapping to the selection of the dominant spectrum and finally to the calculation of the peak shift with an estimated time of only a few minutes.

**SARS-CoV-2 Sensing Performance of HyperSENSE.** We used the HyperSENSE sensor and recorded its response at a very low concentration of SARS-CoV-2 RNA, by measuring the shift in the HSI signal. The EDF-HSI before and after the addition of SARS-CoV-2 RNA to HfNPs-$P_{mix}$ has been displayed in Figure 4. The data show a prominent shift in the HSI signal upon the addition of RNA, revealing the aggregation of the HfNPs conjugated to ssDNA probes. The addition of SARS-CoV-2 RNA at different concentrations leads to the formation of HfNPs of various sizes. Figure 4a−c depict the EDF-HSI of the SARS-CoV-2 RNA ranging from 0.09721 yM to 97.21 fM. This hybridization of the ssDNA probes with the SARS-CoV-2 RNA resulted in an obvious red-shift in the HSI signal even at a low concentration of 0.09721 yoctomolar (yM). The EDF-HSI before and after the addition of SARS-CoV-2 RNA with 0.09721 yM to HfNPs-$P_{mix}$ is displayed in Figure 4e,f. Using the same procedure with the unmodified HfNPs, the shift in the HSI signal is barely detectable at the same copy numbers. The calibration curve of the HyperSENSE (0.09721 yM to 97.21 fM) showed the shift in HSI signal to be linearly proportional to the $\log_{10}$ (RNA copy number) with $R^2$ = 0.884, Figure 4g. Although nonlinear regression provides more flexibility in terms of the curve shape, linear fitting is preferred to generate a standard curve.[35,36] It is simpler to implement the linear curve in the final prototype with low computational cost and can be generated using a smaller number of points. A linear standard curve is also better in the long run when developing a prototype from the HyperSENSE

technology. This can be attributed to the simplicity of back calculating the concentration of an unknown sample using the linear equation when compared to another formula, *e.g.,* quadratic. Linear fitting of the standard curve was performed on the HyperSENSE response toward serially diluted SARS-CoV-2 genomic RNA samples. The limit of detection (LOD) was found to be 0.09721 yM. Based on the IUPAC guidance of a 3:1 signal-to-noise ratio, the limit of detection of the HfNPs-$P_{mix}$ system was determined to be 0.09721 (~0.1) yM. The LOD of the sensor has been calculated using the formula LOD = $3.3 S_Y$/slope, where $S_y$ is the standard deviation of the response. Linear fitting of the standard curve was performed on the HyperSENSE response toward serially diluted SARS-CoV-2 genomic RNA samples. Figure 4h depicts the hyperspectral signal in the absence and the presence of SARS-CoV-2 RNA at 0.09721 yM.

The aggregation of the HfNPs due to the hybridization of the ssDNA with their target RNA leads to the formation of large entities, which explains the shift in the hyperspectral peak. The formation of large entities and HfNP clusters has also been shown by ZetaView, transmission electron microscopy (TEM), and EDF-HSI measurements as shown in Figure 5. The hydrodynamic diameter measurement (Figure 5a) indicates that the hydrodynamic size increases significantly with the addition of RNA from COVID-19 positive samples (confirmed by RT-qPCR with a Ct number of 22.1), while no substantial difference in hydrodynamic size was found after the addition of MERS-CoV viral RNA. EDF-HSI further supports these findings of the formation of large entities upon the addition of SARS-CoV-2 genomic RNA as shown in Figure 5b. TEM images of the HfNPs-$P_{mix}$ in the absence (Figure 5c) as well as in the presence of SARS-CoV-2 RNA (Figure 5d,e) also support our hypothesis regarding the formation of HfNP clusters due to the recognition of the target RNA. When the system was tested using SARS-CoV, influenza A H1N1, and MERS viruses, no significant shift in the HSI signal has been observed and no large entities were formed, as shown in Figure 5f−h, when compared to clinical SARS-CoV-2 RNA (Figure 5i), indicating good selectivity. Our technology does not rely on the size or the shape to estimate the concentration of the virus RNA. Instead, we are relying on reflectance-based spectral signatures to measure the viral RNA concentration. HfNPs were found to have an anhydrous diameter of ~5 nm when observed under TEM. If few particles of the individual particles are close to each other, they will appear as one cluster under the light microscope due to its low resolution, even though in reality they are apart. Therefore, we did not rely on the particle size as a parameter, but instead, we relied on the spectrum obtained from each sample to estimate the viral genetic material concentration. Utilizing the reflectance spectral signature addresses the limitation that may arise due to the poor resolution of the light microscope when investigating nanoparticles.

**Clinical Evaluation of the HyperSENSE Sensor Performance.** To further evaluate the clinical performance of the developed HyperSENSE kit, a blinded study was performed using 66 clinical nasopharyngeal swab samples (48 COVID-19 positive and 18 negative samples), and the results were benchmarked with an FDA-approved COVID-19 RT-qPCR kit. The RT-qPCR detection kit we employed in this study is FDA-approved LABGUN and Applied Biosystems TaqPath COVID-19 Combo kit. These are designed as three target kits (ORF, N1, N2) to confirm the COVID-19
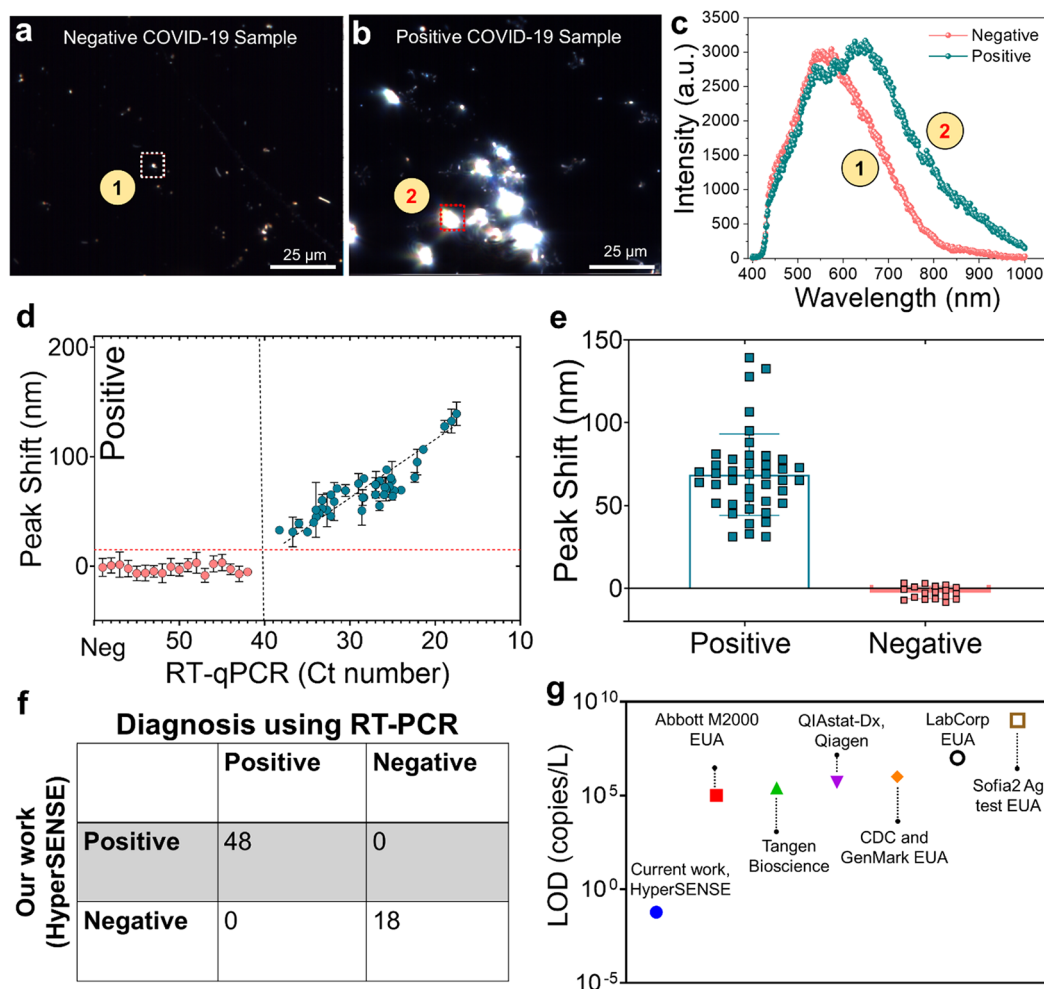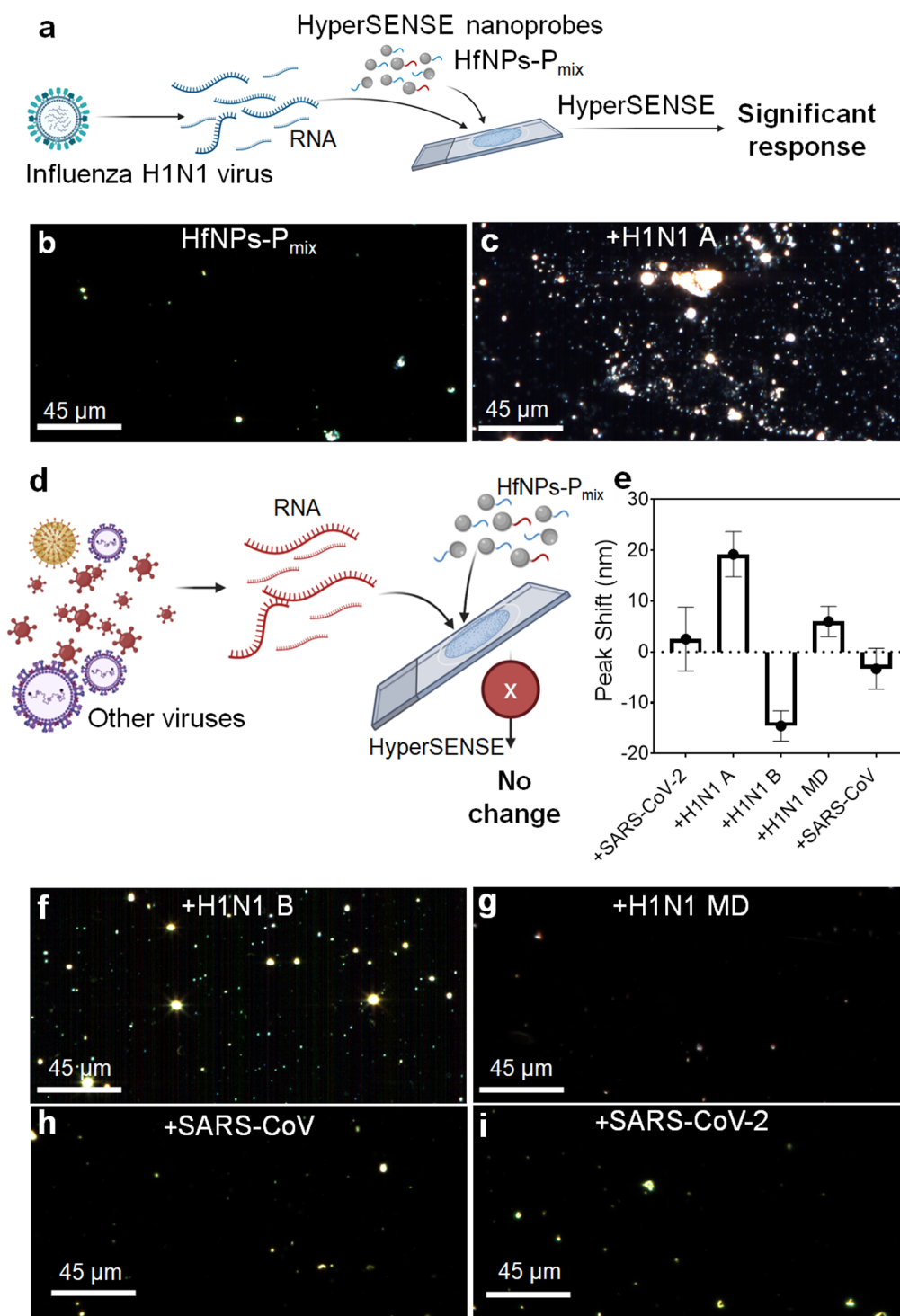
**Figure 6.** Evaluation of the HyperSENSE platform using clinical samples. EDF-HSI of the HfNPs-P$_{mix}$ after the addition of (a) a confirmed COVID-19 negative sample and (b) a confirmed COVID-19 positive sample. The presence of SARS-CoV-2 genetic material leads to the formation of large entities. (c) Hyperspectral signal of the HyperSENSE as a response to positive or negative COVID-19 samples as marked with boxes. A significant shift in the peak wavelength was observed after the addition of the confirmed COVID-19 positive sample. (d) Individual values of the hyperspectral peak shift obtained from the system as a response to the 66 clinical samples with their cycle threshold number (Ct number) obtained from RT-PCR. The peak shift of the positive samples is linearly inversely proportional to the sample's Ct number, Pearson's correlation = $-0.8928$, $R^2 = 0.86$, X intercept > 40 Ct number, indicating its sensitivity. (e) Column plot of the peak shift in nm of the HyperSENSE as a response to 66 COVID-19 clinical samples. (f) Confusion matrix comparing the classification results of HperSENSE as benchmarked to the gold standard RT-PCR. (g) Comparison of the limit of detection obtained using HyperSENSE and other available COVID-19 tests. EUA: emergency used authorization from the Food and Drug Administration. The experiments were performed with experimental repeats of $n = 8$.

diagnosis. Figure 6a,b show the representative hyperspectral imaging of the HfNPs-P$_{mix}$ after the addition of confirmed positive and negative COVID-19 clinical samples. The confirmed COVID-19 positive samples induce the aggregation of the HfNPs due to the specificity of the conjugated ssDNA, which can be seen as a bright large entity shown in Figure 6b, whereas no significant aggregation was observed upon the addition of the negative COVID-19 samples, as shown in Figure 6a. Upon observing the hyperspectra of the large entities' spatial location, the positive sample exhibits a significant peak shift, compared to the negative samples (Figure 6c). Figure 6d illustrates the individual values of the hyperspectral peak shift obtained from the system as a response to the 66 clinical samples with their corresponding Ct values. The HyperSENSE output was found to be linearly proportional with the Ct number, where the curve X intercept is >40 Ct number, confirming the test sensitivity. The shift

obtained in the case of the negative sample is significantly low, and thus the positive COVID-19 cases can easily be distinguished from the negative ones with high accuracy (Figure 6e). The confusion matrix of the classification of the clinical samples as compared to the gold standard methods is shown in Figure 6f.

To further demonstrate the selectivity and sensitivity of the HyperSENSE sensor, we compared our results with previously reported SARS-CoV-2 biosensors, as shown in Figure 6g. Our HyperSENSE-based sensor outperforms all the other conventional biosensors developed for COVID-19 diagnosis. In particular, our sensor can detect as low as 0.09721 yM, indicating the great potential of the nanomaterial when combined with the hyperspectral imaging system in applications such as biosensing, environmental applications, single-molecule biological imaging, and clinical diagnosis.

**Figure 7.** Performance of the HyperSENSE platform toward the detection of the influenza A H1N1 virus and the sensor cross-reactivity. (a) Schematic representation of the HyperSENSE to test influenza A H1N1 samples. EDF-HSI of the HfNPs-Pmix (b) in the absence of samples and (c) after the addition of the influenza A H1N1 sample. (d) Schematic representation of the HyperSENSE to test samples lacking influenza A H1N1 RNA. (e) Peak shift in nm after the addition of SARS-CoV-2, H11N1 A, H1N1 B, H1N1MD, and SARS-CoV viruses, respectively. (f) EDF-HSI after the addition of an influenza B H1N1 sample, (g) an influenza MD H1N1 (Maryland strain) sample, (h) a SARS-CoV sample, and (i) a SARS-CoV-2 sample. The experiments were performed with experimental repeats of $n = 8$.

**Broad Adaptability of the HyperSENSE Sensor for the Detection of Other Pathogens.** The sensing platform we are proposing in this study can be easily and quickly adapted to detect other pathogens. To do so, we only need to redesign ssDNA probes specific to the target pathogen. As a proof of concept, we utilized the HyperSENSE sensor to detect

seasonal influenza A H1N1. The antisense oligonucleotides specific for seasonal influenza A, H1N1, have been conjugated on the surface of HfNPs to develop the HyperSENSE influenza sensor.

A schematic illustration of the workflow of HyperSENSE for influenza detection is shown in Figure 7a. Figure 7b depicts the
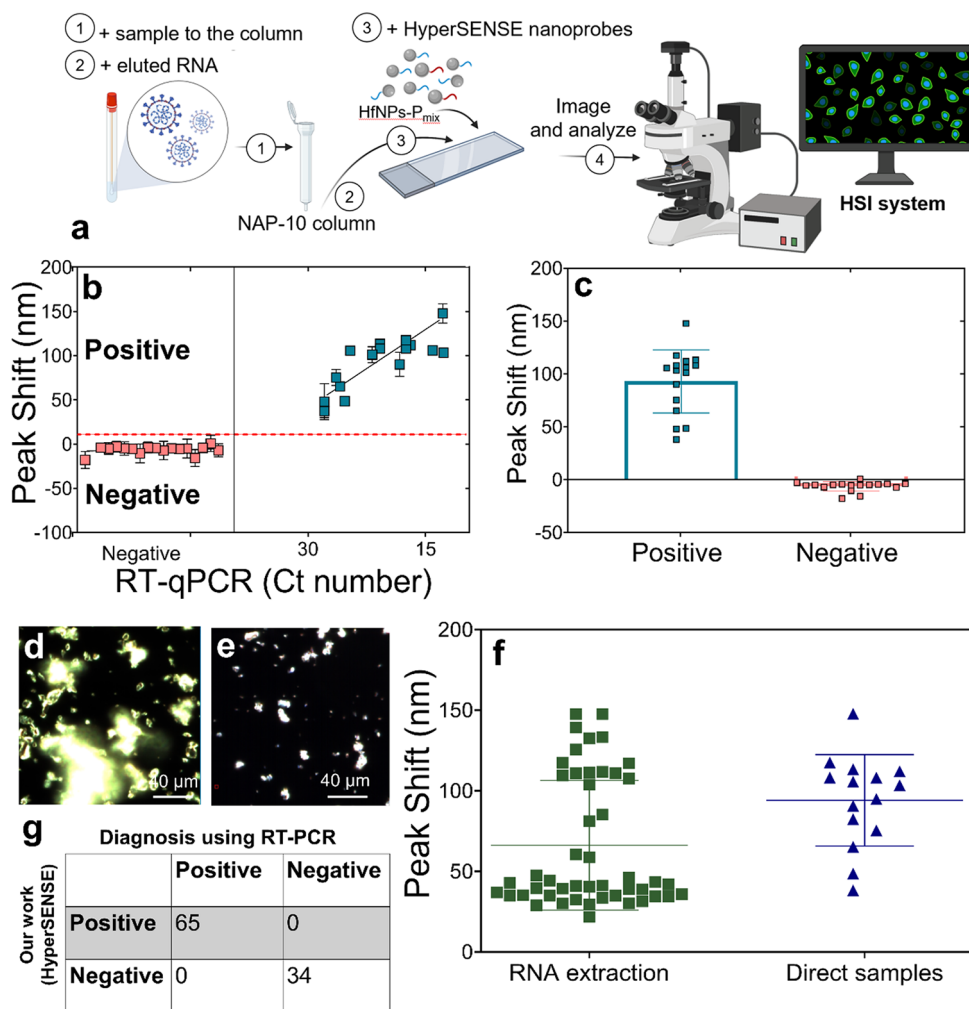
**Figure 8.** SARS-CoV-2 detection from direct clinical samples using HyperSENSE. (a) Clinical samples in VTM were passed through the NAP-10 column and mixed directly with the HfNPs-P$_{mix}$. A total of 33 samples (16 positives and 17 negatives; confirmed by RT-qPCR) were tested using HyperSENSE. (b) Peak shift in the HSI signal as a response to 33 COVID-19 clinical samples as a function of their Ct value as obtained from RT-PCR. Pearson's correlation was found to be −0.8. The positive and negative COVID-19 samples were correctly distinguished from each other (threshold = 11). (c) Column plot of the peak shift in nm obtained from HyperSENSE as a response to two groups, positive and negative COVID-19 samples. (d) EDF-HSI of the COVID-19 positive and (e) negative samples. Large entities were formed when a positive sample was tested using HyperSENSE. (f) Column plot of the peak shift in nm as obtained from 99 clinical samples tested using HyperSENSE using both protocols for sample preparation. (g) Confusion matrix comparing the classification results of HyperSENSE as benchmarked to the gold standard RT-PCR of all the tested clinical samples. The experiments were performed with experimental repeats of $n = 8$.

EDF-HSI of the conjugated HfNPs in the absence of the target. However, upon the addition of the influenza A H1N1 sample, large aggregates have been observed (Figure 7c). The cross-reactivity of the HyperSENSE sensor has been tested using H1N1 B, H1N1MD (Maryland strain), SARS-CoV, and SARS-CoV-2 viral strains, as illustrated in the schematic representation in Figure 7d. In terms of the shift in the HSI signal, the maximum shift was observed in the case of H1N1 A, confirming the specificity of the developed test (Figure 7e). Figure S12 shows the spectra of the unbound HfNPs functionalized with ASOs specific to the influenza A H1N1 genetic materials and the hyperspectral signal associated with the H1N1 A, H1N1 B, H1N1 MD, SARS-CoV, and SARS-CoV-2 biological sample. The data show a significant right shift in the reflectance hyperspectral signal in the presence of its target (*i.e.*, H1N1 A), whereas no obvious shift in the spectra was observed in the case of the off-target viruses including SARS-CoV, H1N1MD, and SARS-CoV-2, whereas the H1N1

B spectrum exhibits a shift from the unbound one to the left, which can be easily distinguishable from H1N1 A. This can be eliminated by removing the values below zero by applying a thresholding technique to the sensor data. This will also help in discriminating H1N1 A from H1N1 B samples. This confirms that the test does not have any cross-reactivity toward other viruses. Specificity describes a biosensor's ability to differentiate between target and nontargeted biological entities in a sample. Therefore, the specificity of the HyperSENSE was found to be 100%. Minimal aggregations were observed in the case of H1N1 B, whereas no significant aggregation was observed in the case of other samples, as shown in Figure 7f−i.

Our data obtained from the HyperSENSE platform confirmed the excellent sensitivity and specificity of the biosensor toward COVID-19 detection even at a very low concentration. But we realized that the RNA extraction step can add an extra burden toward the real-time detection of the pathogens, as it can be a time-consuming and laborious

L

process. Therefore, we have modified the HyperSENSE workflow to compromise the RNA extraction step. The updated HyperSENSE workflow for SARS-CoV-2 detection using direct clinical samples is shown in Figure 8a. The sample will be collected from the patient in VTM and then passed through the NAP-10 column for RNA extraction. This process takes around 2 min only. Next, the extract will be mixed with HfNPs-$P_{mix}$ and imaged using the hyperspectral imaging system. The data will be further analyzed to identify the shift in the light scattering to assign the sample as either positive or negative COVID-19. The updated HyperSENSE workflow has been validated using 33 clinical samples obtained from patients with confirmed COVID-19 in the state of Maryland and Florida as diagnosed by RT-qPCR. The 33 samples were processed as shown in Figure 8a, where the as-collected nasopharyngeal swab samples in VTM passed through the NAP-10 column and mixed directly with the HfNPs-$P_{mix}$ and were imaged using the HSI system. The positive predictive agreement and negative predictive agreement of the Hyper-SENSE assay are ∼100% (33 out of 33) relative to the RT-qPCR results (Figure 8b). The threshold of the peak shift value has been selected to maximize the two-class separation as shown in Figure S13. The peak shifts obtained from the 33 clinical samples tested using HyperSENSE of the two groups (positive and negative COVID-19) were found to be significantly different (Figure 8c), and representative images of EDF-HSI of both confirmed positive and negative cases are shown in Figure 8d,e. Figure 8f shows the individual outputs of HyperSENSE from 99 samples tested using two protocols of sample prepreparation (RNA extraction, direct sample). The confusion matrix of COVID-19 diagnosis using HyperSENSE of all the tested clinical samples is shown in Figure 8g. The test achieves 100% sensitivity, specificity, and accuracy while providing low LOD.

Apart from the strong interaction between the HfNP-$P_{mix}$ and the target RNA, the HfNPs being a strong light-scattering agent also contributes to the high sensitivity of the HSI. It was observed that the HyperSENSE sensor has a limit of detection of 0.06 copy/liter, *i.e.*, 0.09 yM, representing the highest sensitivity described so far for SARS-CoV-2 RNA detection.

To control the rapid spread of SARS-CoV-2 requires simple, rapid, and sensitive diagnostic tests.[37−42] However, conventional approaches have their inherent limitations. For example, culture-based approaches are time-consuming (more than 24 h), whereas PCR-based methods including real-time PCR require complex equipment, trained staff, and expensive reagents in addition to being a time-consuming process. Several isothermal amplification methods have been proposed for SARS-CoV-2 detection.[43−46] However, spurious by-products are an inherent limitation that leads to high false positives. Nucleic acid amplification-free approaches, on the other hand, provide advantages for rapid tests at the patient's point of care. In this scenario, hyperspectral-based imaging provides a wealth of information that has been used to detect SARS-CoV-2. In contrast, the HSI diagnostic framework meets all of the desirable criteria for an on-site diagnosis of COVID-19, including a faster turnover period (∼few minutes), a low detection limit (∼0.06 copy/L), and low-cost reagents that can be easily adapted to detect other pathogens.

The HyperSENSE platform can be translated into a POC system by utilizing a portable hyperspectral scanner for output readout.[47] HyperSENSE combines all components into a single pot, where the readings can be read instantaneously using specially developed probes. Also, with the robustness of the probes, the architecture is comprehensive and straightforward, allowing the platform to be flexible. Thus, the applicability of the HyperSENSE platform can also be applied to evolving pathogens, as exemplified by the successful design of the SARS-CoV-2 and influenza H1N1 A virus detection platform.

The ssDNA for the detection of SARS-CoV-2 is designed to target multiple locations of the target gene simultaneously.[17,23] This allows the aggregation of nanoparticles through the hybridization of the probe with the target RNA. The antisense oligonucleotide sequences have been carefully designed to minimize any secondary structure formation on their own and that maximizes RNA−DNA hybridization by considering their target binding energy and binding disruption energy.[17,23] The strong hybridization between the ssDNA and target RNA enabled high sensitivity and selectivity, whereas HSI further allows achieving a LOD lower than yM concentration of the RNA.

We expect HyperSENSE to have a broad range of applications for pathogen detection ranging from clinical diagnosis to environmental applications.[17,23,27,48] First, Hyper-SENSE can be effectively deployed in the initial mass surveillance of infectious diseases in high clustered areas. With a short processing time, easy components, and the potential to automate the whole procedure, HyperSENSE is an ideal candidate for a fast and cost-effective diagnostic test that can be run by people with limited experience. On the basis of our study data, we found that the accuracy, sensitivity, and specificity of the sensor are fully dependent on the spectral information and not on the size or shape observation. Therefore, the use of a microscopy system is not a necessity when a point-of-care platform is envisioned. We anticipate that a hand-held hyperspectral scanner that can record the reflectance spectrum from the sample can be used to propose a HyperSENSE POC prototype system. We may also envision a "snapshot"-type (nonscanning) hyperspectral method for capturing spectral images during a single integration time of a detector array, which may simplify the data processing and improve the image processing time.

Thus, HyperSENSE can be implemented in laboratories for mass screening as well as a field-deployable system using a portable hand-held hyperspectral scanner. Due to the versatility of the test operation principle and the availability of a portable hyperspectral scanner, the test can be built into a paper-based or lateral flow-based disposable platform.[49−51] Moreover, the test has the potential to expand its applicability to cover emerging pathogens due to the simplicity of designing the target ssDNA probes and integrating them with the reporter nanoparticles (HfNPs), which confirms the wide adaptability of the HyperSENSE platform.

It is worth mentioning that the hyperspectral scans demand large data storage due to capturing a full light spectrum ranging from visible to near-infrared at each pixel. This provides a multidimensional data set with a size that may exceed a few megabytes. Moreover, fast computational units and sensitive detectors are required to efficiently analyze hyperspectral data. These factors may increase the cost for both storing and analysis of the hyperspectral data. Therefore, innovative approaches such as advanced programming skills and computational algorithms for processing and analyzing hyperspectral data are required to address these limitations. COVID-19 is a deadly and complex disease.[33,52,53] A major challenge in

managing the progression of COVID-19 is a lack of consistent monitoring of the time-dependent inflammatory response and the interconnected thrombotic response.[54,55] More than 30% of patients suffering from COVID-19 will develop secondary complications.[56,57] Multiple studies have shown that these complications peak weeks after peak COVID-19 activity in a region.[58] At least half of these patients are RT-PCR negative, and many patients with a clear epidemiologic link to COVID-19 are both RT-PCR and antibody negative.[59] Patients who were recently infected with SARS-CoV-2 have detectable viral particles upon sensitive testing.[60] However, the current clinical testing is set to high specificity, excluding many samples that have trace quantities of virus.[61] Sensitive viral testing may identify recent active respiratory infection with SARS-CoV-2.[62] Thus, HyperSENSE provides a solution to diagnose COVID-19 at its earliest by addressing the limitation associated with other available tests.

## CONCLUSION

In this work, we demonstrated the successful application of HyperSENSE to two viruses, using minimal modification. From a theoretical perspective, HyperSENSE can be designed to detect any pathogen as long as we know the sequence of the target nucleic acid. By this, HyperSENSE outperforms the antigen-based tests in rapidly responding to an outbreak of infectious diseases. Further, the synthesis of ssDNA is low cost and scalable when compared to animal antibody production. Therefore, the HyperSENSE scalability and mass production is much easier when compared to antibody-based diagnostic kits. In this work, we demonstrate the successful development of a powerful diagnostic technology for RNA detection with a very high sensitivity up to ∼0.1 yM. The technology offers short turn-around time, high sensitivity, specificity, and ease-of-use, with the possibility for detecting other types of pathogens. Thus, the design of HyperSENSE can be simple and can be quickly redesigned to target any emerging infectious diseases.

## MATERIALS AND METHODS

**Synthesis of HfNPs-COOH.** The confined sol−gel method has been carried out in microemulsion to synthesize the HfNPs based on the previously published protocol from our group.[34] First, 17.25 g of IGEPAL CO-520 was added to 150 mL of cyclohexane. Next, 5.625 mL of ethanol and 1.875 mL of sodium hydroxide (75 mM) were added to the mixture. The mixture was stirred at 65 °C for approximately 10 min until it is homogeneous. Next, 375 $\mu$L of water was added dropwise to form the microemulsion. Finally, 0.8071 g of hafnium ethoxide was added, and the reaction was allowed to run to completion overnight. The particles were washed three times with methanol and dried in a vacuum oven to be used for the next step. To tune the HfNPs' surface functionality, 250 mg of HfNPs was reacted with 3-(aminopropyl)triethoxysilane in 35 mL of toluene at 110 °C. The reaction was run for 12 h under reflux with $N_2$ conditions. The particles were then washed three times with toluene and dried for the next step. Next, 100 mg of the HfNPs-$NH_2$ particles was reacted with succinic anhydride in 11 mL of dimethylformamide (DMF) for 24 h at room temperature (25 °C). The particles were then washed and dried properly to be used in the conjugation step.

**Design of Antisense Oligonucleotides.** The target *N-gene* sequence of SARS-CoV-2, as mentioned in the Supporting Information, was supplied to software, Soligo,[63] for statistical folding of nucleic acids and studies of regulatory RNAs. The ASOs were predicted to maintain the folding temperature as 37 °C and ionic conditions of 1 M sodium chloride for a preferred length of ASO as 20 nucleotide bases. The filter criteria were set as follows: (1) The GC% will be within 40% to 60%; (2) the target sequences with

GGGG will be eliminated; (3) the average unpaired probability of the ASOs should be within ≥0.5 for target site nucleotides; (4) among sites satisfying criteria 1−3, the top 20 will be considered with the highest average unpaired probability. In order to reduce the number of reported sites, the average unpaired probability was also used in filter criteria 3 and 4. The disruption energy calculation in the Web servers was also optimized accordingly. Finally, the binding energies of the ASOs were also compared with the target sequence to decide on the sequences.

**Conjugation of ASO to the HfNPs.** The EDC/NHS coupling reaction has been used to functionalize the HfNPs-COOH to ASO-$NH_2$. In a typical reaction, either 2.5 or 5 $\mu$L of ASO-$NH_2$ (200 $\mu$M in Tris buffer) was added to 1 mL of HfNPs-COOH (20 mg/mL) to form the 0.5 $\mu$M HfNPs-ASO (low probe density) or 1 $\mu$M HfNPs-ASO (high probe density), respectively. The reaction takes place overnight under stirring conditions at room temperature (25 ± 1 °C). Next, the solution was centrifuged at 12 000 rcf for 20 min, and the supernatant was discarded to remove any unreacted EDC/NHS. Finally, the particles conjugated to ASO1 and ASO2 were mixed in equal amounts to form HfNPs-$P_{mix}$ and sonicated for homogenization. The particle mixture was diluted to a final concentration of 1 mg/mL and stored at 4 °C for further use. The particles were vortexed and sonicated adequately before each use.

**HyperSENSE Sample Preparation, Data Recording, and Processing.** Briefly, the test sample were mixed with the HfNPs-$P_{mix}$ in 1:1 ratio, and 5 $\mu$L of the mixture was drop cast onto a glass slide and covered by a coverslip. The sample was then imaged instantaneously. An enhanced dark-field illumination system (Cyto-Viva, Auburn, AL, USA) has been used to capture the HSI images throughout this work. The tungsten−halogen light source is used as an illumination system, which has been attached to an Olympus microscope for image capturing. The scattering light was consolidated with either a 60× or a 100× oil immersion Olympus objective. For the hyperspectral imaging method, the scattering signal was transferred by a narrow slit and was then separated by the gratings into the spectrograph and collected by a CCD (PIXIS-400BR, Princeton Instruments). Based on the hyperspectral data set, the spectrum of scattering at each pixel can be obtained using the CytoViva software program (ENVI 4.8). Collecting a spectrum from a particular area involves two main processes. First, identifying the region of interest (ROI) and building the hyperspectral image by normalizing the hyperspectral signal to the dark current image. Second, the 1D hyperspectral signals were collected from the HSI at certain ROIs and stored to form a spectral library. The SAM algorithm is used to generate mapping images to determine the predominant spectral signature. The spectra of the predominant region were then further analyzed to identify the peak value. Next, the peak shift of the sample with respect to the signal from bare HfNPs-$P_{mix}$ will be identified as an output parameter. Spectral data were analyzed using Origin software to identify the peak and the peak shift in the case of each sample. Around 16 ROIs have been processed for each sample.

**Physicochemical Characterizations.** To visualize the morphology of the NPs, the hydrodynamic diameters of the individually ASO-capped nanoparticles and the composite nanoparticles were monitored on a particle tracking analyzer (Zetaview Particle Metrix). The chamber of the machine was properly cleaned prior to each measurement. Further, the as-synthesized nanoparticles before and after the addition of RNA were investigated under the transmission electron microscope (FEI Tecnai T12). The tungsten filament was used as the electron optics, and the voltage was kept constant at 80 kV. A sample droplet was spotted onto a carbon-coated copper grid (400 mesh) and allowed to stay there for about 10 min before being removed.

**Isolation of RNA.** Severe acute respiratory syndrome-related coronavirus (SARS-CoV-2), isolate USA-WA1/2020, was isolated from an oropharyngeal swab of a patient with a respiratory illness. The sample, NR-52287, as obtained from BEI Resources, NIAID, NIH, consists of a crude preparation of cell lysate and supernatant from *Cercopithecus aethiops* kidney epithelial cells (Vero E6; ATCC CRL-1586) infected with SARS-CoV-2, isolate USA-WA1/2020, that was

gamma-irradiated ($5 \times 10^6$ rad) on dry ice. The sample, NR-50549, as obtained from BEI Resources, NIAID, NIH, consists of a gamma-irradiated cell lysate and supernatant from Vero cells infected with MERS-CoV, EMC/2012. The total RNA was then extracted and purified for the viral RNA from the cellular lysate with a commercially available kit. The following reagents were also obtained through BEI Resources, NIAID, NIH: (i) swine influenza A (H1N1) real-Time RT-PCR assay, NR-15577; (ii) genomic RNA from influenza A virus, A/gull/Maryland/704/1977 (H13N6), NR-43019; (iii) genomic RNA from influenza B virus, B/Ohio/01/2005 (Victoria lineage), NR-43753; and (iv) quantitative PCR (qPCR) control RNA from inactivated SARS coronavirus, Urbani, NR-52346.

**Preparation of Clinical Samples.** The clinical samples tested in this work were collected as part of the registered protocols approved by the Institutional Review Board of the University of Maryland, Baltimore. Samples of nasopharyngeal swabs were stored in viral transfer media, and then the samples were stored at −80 °C for future use. The total RNA was then extracted and purified for the viral RNA from the cellular lysate with a commercially available kit.

**Direct Clinical Sample Testing.** A NAP-10 column was equilibrated as per the manufacturer's protocol. A 40 μL amount of the nasopharyngeal swab sample in VTM was mixed with 20 μL of guanidine isothiocyanate containing lysis buffer and added to the NAP-10 column. A 1 mL amount of RNase-free water was added to the column, and the eluted liquid containing the RNA was collected. Next, 5 μL of the eluted liquid was mixed with 5 μL of HfNPs-P$_{mix}$; then 5 μL was deposited on a glass slide with a coverslip for HSI imaging.

**Docking Studies.** The chemical structures were first energy minimized using a general *ab initio* quantum chemistry package, the General Atomic and Molecular Electronic Structure System (GAMESS) program.[64] We used the MINI functional as Huzinaga's 3 Gaussian minimal basis set with Pople N31 for the polar groups while performing the density functional theory calculations. These energy-minimized structures were then undertaken for docking studies using AutoDock 4.0 software.[65−67]

**Density Functional Theory Calculations.** The chemical structures were initially energy-optimized, and the HOMO−LUMO surfaces were then calculated from their energy-minimized geometries using a general *ab initio* quantum chemistry package (GAMESS) as described above.[27,64] The highest occupied molecular orbital energy ($E_{HOMO}$), the lowest unoccupied molecular orbital energy ($E_{LUMO}$), and the energy gap between $E_{LUMO}$ and $E_{HOMO}$ were calculated and represented as $\Delta E_{LUMO-HOMO}$.

## ASSOCIATED CONTENT

### ⓢ Supporting Information

The Supporting Information is available free of charge at https://pubs.acs.org/doi/10.1021/acsnano.1c05226.

Supplementary Data 1, the sequence of the nucleocapsid phosphoprotein; Tables S1, sequences considered for theoretical calculations, and Figures S1−S13 (PDF)

## AUTHOR INFORMATION

### Corresponding Author

**Dipanjan Pan** − *Bioengineering Department, The University of Illinois at Urbana−Champaign, Urbana, Illinois 61801, United States; Departments of Diagnostic Radiology and Nuclear Medicine and Pediatrics, Center for Blood Oxygen Transport and Hemostasis, University of Maryland Baltimore School of Medicine, Baltimore, Maryland 21201, United States; Department of Chemical, Biochemical and Environmental Engineering, University of Maryland Baltimore County, Baltimore, Maryland 21250, United States;* ⓞ orcid.org/0000-0003-0175-4704; Email: dipanjan@som.umaryland.edu

### Authors

**Maha Alafeef** − *Bioengineering Department, The University of Illinois at Urbana−Champaign, Urbana, Illinois 61801, United States; Departments of Diagnostic Radiology and Nuclear Medicine and Pediatrics, Center for Blood Oxygen Transport and Hemostasis, University of Maryland Baltimore School of Medicine, Baltimore, Maryland 21201, United States; Biomedical Engineering Department, Jordan University of Science and Technology, Irbid 22110, Jordan; Department of Chemical, Biochemical and Environmental Engineering, University of Maryland Baltimore County, Baltimore, Maryland 21250, United States*

**Parikshit Moitra** − *Departments of Diagnostic Radiology and Nuclear Medicine and Pediatrics, Center for Blood Oxygen Transport and Hemostasis, University of Maryland Baltimore School of Medicine, Baltimore, Maryland 21201, United States;* ⓞ orcid.org/0000-0002-7679-7859

**Ketan Dighe** − *Departments of Diagnostic Radiology and Nuclear Medicine and Pediatrics, Center for Blood Oxygen Transport and Hemostasis, University of Maryland Baltimore School of Medicine, Baltimore, Maryland 21201, United States; Department of Chemical, Biochemical and Environmental Engineering, University of Maryland Baltimore County, Baltimore, Maryland 21250, United States*

Complete contact information is available at:
https://pubs.acs.org/10.1021/acsnano.1c05226

### Notes

The authors declare the following competing financial interest(s): D.P. is the founder of three University based start-ups. None of these entities however supported this work.

## REFERENCES

(1) Gandhi, M.; Yokoe, D. S.; Havlir, D. V. Asymptomatic Transmission, the Achilles' Heel of Current Strategies to Control COVID-19. *N. Engl. J. Med.* **2020**, *382* (22), 2158−2160.

(2) Huang, J.; Zhao, L. A High-Throughput Strategy for COVID-19 Testing Based on Next-Generation Sequencing. 2020. *medRxiv* **2021**, DOI: 10.1101/2020.06.12.20129718.

(3) Wilder-Smith, A.; Chiew, C. J.; Lee, V. J. Can We Contain the COVID-19 Outbreak with the Same Measures as for SARS? *Lancet Infect. Dis.* 2020, 20 (5), e102−e107.

(4) Subbarao, K.; Mahanty, S. Respiratory Virus Infections: Understanding COVID-19. *Immunity* 2020, 52 (6), 905−909.

(5) Dhar Chowdhury, S.; Oommen, A. M. Epidemiology of COVID-19. *Journal of Digestive Endoscopy* 2020, 11 (01), 03−07.

(6) Cuadrado-Payán, E.; Montagud-Marrahi, E.; Torres-Elorza, M.; Bodro, M.; Blasco, M.; Poch, E.; Soriano, A.; Piñeiro, G. J. SARS-CoV-2 and Influenza Virus Co-Infection. *Lancet* 2020, 395 (10236), No. e84.

(7) Lee, S.; Kim, T.; Lee, E.; Lee, C.; Kim, H.; Rhee, H.; Park, S. Y.; Son, H.-J.; Yu, S.; Park, J. W.; Choo, E. J.; Park, S.; Loeb, M.; Kim, T. H. Clinical Course and Molecular Viral Shedding among Asymptomatic and Symptomatic Patients with SARS-CoV-2 Infection in a Community Treatment Center in the Republic of Korea. *JAMA Internal Medicine* 2020, 180 (11), 1447−1452.

(8) Yuen, K.-S.; Ye, Z.-W.; Fung, S.-Y.; Chan, C.-P.; Jin, D.-Y. SARS-CoV-2 and COVID-19: The Most Important Research Questions. *Cell Biosci.* 2020, 10, 40−41.

(9) Argyropoulos, K. V.; Serrano, A.; Hu, J.; Black, M.; Feng, X.; Shen, G.; Call, M.; Kim, M. J.; Lytle, A.; Belovarac, B.; Vougiouklakis, T.; Lin, L. H.; Moran, U.; Heguy, A.; Troxel, A.; Snuderl, M.; Osman, I.; Cotzia, P.; Jour, G. Association of Initial Viral Load in Severe Acute Respiratory Syndrome Coronavirus 2 (SARS-CoV-2) Patients with Outcome and Symptoms. *Am. J. Pathol.* 2020, 190 (9), 1881−1887.

(10) Fajnzylber, J.; Regan, J.; Coxen, K.; Corry, H.; Wong, C.; Rosenthal, A.; Worrall, D.; Giguel, F.; Piechocka-Trocha, A.; Atyeo, C.; Fischinger, S.; Chan, A.; Flaherty, K. T.; Hall, K.; Dougan, M.; Ryan, E. T.; Gillespie, E.; Chishti, R.; Li, Y.; Jilg, N.; et al. SARS-CoV-2 Viral Load Is Associated with Increased Disease Severity and Mortality. *Nat. Commun.* 2020, 11 (1), 5493.

(11) Xu, T.; Chen, C.; Zhu, Z.; Cui, M.; Chen, C.; Dai, H.; Xue, Y. Clinical Features and Dynamics of Viral Load in Imported and Non-Imported Patients with COVID-19. *Int. J. Infect. Dis.* 2020, 94, 68−71.

(12) Cevik, M.; Tate, M.; Lloyd, O.; Maraolo, A. E.; Schafers, J.; Ho, A. SARS-CoV-2, SARS-CoV, and MERS-CoV Viral Load Dynamics, Duration of Viral Shedding, and Infectiousness: A Systematic Review and Meta-Analysis. *Lancet Microbe* 2021, 2 (1), e13−e22.

(13) *Transmission of SARS-CoV-2: Implications for Infection Prevention Precautions*. https://www.who.int/news-room/commentaries/detail/transmission-of-sars-cov-2-implications-for-infection-prevention-precautions (accessed Feb 04, 2021).

(14) Patrozou, E.; Mermel, L. A. Does Influenza Transmission Occur from Asymptomatic Infection or Prior to Symptom Onset? *Public Health Rep.* 2009, 124 (2), 193−196.

(15) Ip, D. K. M.; Lau, L. L. H.; Leung, N. H. L.; Fang, V. J.; Chan, K.-H.; Chu, D. K. W.; Leung, G. M.; Peiris, J. S. M.; Uyeki, T. M.; Cowling, B. J. Viral Shedding and Transmission Potential of Asymptomatic and Paucisymptomatic Influenza Virus Infections in the Community. *Clin. Infect. Dis.* 2016, 64 (6), 736−742.

(16) Nguyen-Van-Tam, J. S.; Killingley, B.; Enstone, J.; Hewitt, M.; Pantelic, J.; Grantham, M. L.; Bueno De Mesquita, P. J.; Lambkin-Williams, R.; Gilbert, A.; Mann, A.; Forni, J.; Noakes, C. J.; Levine, M. Z.; Berman, L.; Lindstrom, S.; Cauchemez, S.; Tellier, R.; Milton, D. K. Minimal Transmission in an Influenza a (H3N2) Human Challenge-Transmission Model within a Controlled Exposure Environment. *PLoS Pathog.* 2020, 16 (7), e1008704−e1008703.

(17) Alafeef, M.; Dighe, K.; Moitra, P.; Pan, D. Rapid, Ultrasensitive, and Quantitative Detection of SARS-CoV-2 Using Antisense Oligonucleotides Directed Electrochemical Biosensor Chip. *ACS Nano* 2020, 14 (12), 17028−17045.

(18) Sethuraman, N.; Jeremiah, S. S.; Ryo, A. Interpreting Diagnostic Tests for SARS-CoV-2. *JAMA* 2020, 323 (22), 2249−2251.

(19) Yoon, J.; Joseph, J.; Waterhouse, D. J.; Luthman, A. S.; Gordon, G. S. D.; di Pietro, M.; Januszewicz, W.; Fitzgerald, R. C.; Bohndiek, S. E. A Clinically Translatable Hyperspectral Endoscopy (HySE)

System for Imaging the Gastrointestinal Tract. *Nat. Commun.* 2019, 10 (1), 1902.

(20) Hadoux, X.; Hui, F.; Lim, J. K. H.; Masters, C. L.; Pebay, A.; Chevalier, S.; Ha, J.; Loi, S.; Fowler, C. J.; Rowe, C.; Villemange, V. L.; Taylor, E. N.; Fluke, C.; Soucy, J. P.; Lesage, F.; Sylvestre, J. P.; Rosa-Neto, P.; Mathotaarachchi, S.; Gauthie, S.; Nasreddine, Z. S.; et al. Non-Invasive *in Vivo* Hyperspectral Imaging of the Retina for Potential Biomarker Use in Alzheimer's Disease. *Nat. Commun.* 2019, 10 (1), 4227.

(21) Yesilkoy, F.; Arvelo, E. R.; Jahani, Y.; Liu, M.; Tittl, A.; Cevher, V.; Kivshar, Y.; Altug, H. Ultrasensitive Hyperspectral Imaging and Biodetection Enabled by Dielectric Metasurfaces. *Nat. Photonics* 2019, 13 (6), 390−396.

(22) Nevala, N. E.; Baden, T. A Low-Cost Hyperspectral Scanner for Natural Imaging and the Study of Animal Colour Vision above and under Water. *Sci. Rep.* 2019, 9 (1), 10799.

(23) Moitra, P.; Alafeef, M.; Dighe, K.; Frieman, M. B.; Pan, D. Selective Naked-Eye Detection of SARS-CoV-2 Mediated by *N Gene* Targeted Antisense Oligonucleotide Capped Plasmonic Nano-particles. *ACS Nano* 2020, 14 (6), 7617−7627.

(24) Ravina; Mohan, H.; Gill, P. S.; Kumar, A. Hemagglutinin Gene Based Biosensor for Early Detection of Swine Flu (H1N1) Infection in Human. *Int. J. Biol. Macromol.* 2019, 130, 720−726.

(25) Ding, X. R.; Yang, J.; Lu, D. D.; Li, Q. J.; Zhang, Z. Y.; Zhou, Z.; Wang, S. Q. Delivery System Targeting Hemagglutinin of Influenza Virus A to Facilitate Antisense-Based Anti-H1N1 Therapy. *Bioconjugate Chem.* 2017, 28 (7), 1842−1849.

(26) Shi, W.; Koo, D. E. S.; Kitano, M.; Chiang, H. J.; Trinh, L. A.; Turcatel, G.; Steventon, B.; Arnesano, C.; Warburton, D.; Fraser, S. E.; Cutrale, F. Pre-Processing Visualization of Hyperspectral Fluorescent Data with Spectrally Encoded Enhanced Representations. *Nat. Commun.* 2020, 11 (1), 726.

(27) Misra, S. K.; Ostadhossein, F.; Daza, E.; Johnson, E. V.; Pan, D. Hyperspectral Imaging Offers Visual and Quantitative Evidence of Drug Release from Zwitterionic-Phospholipid-Nanocarbon When Concurrently Tracked in 3D Intracellular Space. *Adv. Funct. Mater.* 2016, 26 (44), 8031−8041.

(28) Zhu, B.; Johansen, V. E.; Kamita, G.; Guidetti, G.; Bay, M. M.; Parton, T. G.; Frka-Petesic, B.; Vignolini, S. Hyperspectral Imaging of Photonic Cellulose Nanocrystal Films: Structure of Local Defects and Implications for Self-Assembly Pathways. *ACS Nano* 2020, 14 (11), 15361−15373.

(29) Barella, M.; Violi, I. L.; Gargiulo, J.; Martinez, L. P.; Goschin, F.; Guglielmotti, V.; Pallarola, D.; Schlücker, S.; Pilo-Pais, M.; Acuna, G. P.; Maier, S. A.; Cortés, E.; Stefani, F. D. *In Situ* Photothermal Response of Single Gold Nanoparticles through Hyperspectral Imaging Anti-Stokes Thermometry. *ACS Nano* 2021, 15 (2), 2458−2467.

(30) Alafeef, M.; Dighe, K.; Pan, D. Label-Free Pathogen Detection Based on Yttrium-Doped Carbon Nanoparticles up to Single-Cell Resolution. *ACS Appl. Mater. Interfaces* 2019, 11 (46), 42943−42955.

(31) Schwartz-Duval, A. S.; Konopka, C. J.; Moitra, P.; Daza, E. A.; Srivastava, I.; Johnson, E. V.; Kampert, T. L.; Fayn, S.; Haran, A.; Dobrucki, L. W.; Pan, D. Intratumoral Generation of Photothermal Gold Nanoparticles through a Vectorized Biomineralization of Ionic Gold. *Nat. Commun.* 2020, 11 (1), 4530.

(32) Pan, D.; Kim, B.; Wang, L. V.; Lanza, G. M. A Brief Account Of Nanoparticle Contrast Agents For Photoacoustic Imaging. *WIREs Nanomedicine and Nanobiotechnology* 2013, 5 (6), 517−543.

(33) Qiu, G.; Gai, Z.; Tao, Y.; Schmitt, J.; Kullak-Ublick, G. A.; Wang, J. Dual-Functional Plasmonic Photothermal Biosensors for Highly Accurate Severe Acute Respiratory Syndrome Coronavirus 2 Detection. *ACS Nano* 2020, 14 (5), 5268−5277.

(34) Ostadhossein, F.; Misra, S. K.; Tripathi, I.; Kravchuk, V.; Vulugundam, G.; LoBato, D.; Selmic, L. E.; Pan, D. Dual Purpose Hafnium Oxide Nanoparticles Offer Imaging Streptococcus Mutans Dental Biofilm and Fight It *in Vivo* via a Drug Free Approach. *Biomaterials* 2018, 181, 252−267.

(35) Perrin, C. L. Linear or Nonlinear Least-Squares Analysis of Kinetic Data? *J. Chem. Educ.* **2017**, *94* (6), 669−672.

(36) Fong, Y.; Yu, X. Transformation Model Choice in Nonlinear Regression Analysis of Fluorescence-Based Serial Dilution Assays. *Stat Biopharm Res.* **2016**, *8* (1), 1−11.

(37) Cheong, J.; Yu, H.; Lee, C. Y.; Lee, J.-u.; Choi, H.-J.; Lee, J.-H.; Lee, H.; Cheon, J. Fast Detection of SARS-CoV-2 RNA *via* the Integration of Plasmonic Thermocycling and Fluorescence Detection in a Portable Device. *Nature Biomedical Engineering* **2020**, *4* (12), 1159−1167.

(38) Seo, G.; Lee, G.; Kim, M. J.; Baek, S.-H.; Choi, M.; Ku, K. B.; Lee, C.-S.; Jun, S.; Park, D.; Kim, H. G.; Kim, S.-J.; Lee, J.-O.; Kim, B. T.; Park, E. C.; Kim, S. I. Rapid Detection of COVID-19 Causative Virus (SARS-CoV-2) in Human Nasopharyngeal Swab Specimens Using Field-Effect Transistor-Based Biosensor. *ACS Nano* **2020**, *14* (4), 5135−5142.

(39) Woo, C. H.; Jang, S.; Shin, G.; Jung, G. Y.; Lee, J. W. Sensitive Fluorescence Detection of SARS-CoV-2 RNA in Clinical Samples *via* One-Pot Isothermal Ligation and Transcription. *Nature Biomedical Engineering* **2020**, *4* (12), 1168−1179.

(40) Quer, G.; Radin, J. M.; Gadaleta, M.; Baca-Motes, K.; Ariniello, L.; Ramos, E.; Kheterpal, V.; Topol, E. J.; Steinhubl, S. R. Wearable Sensor Data and Self-Reported Symptoms for COVID-19 Detection. *Nat. Med.* **2021**, *27* (1), 73−77.

(41) Tong, A.; Sorrell, T. C.; Black, A. J.; Caillaud, C.; Chrzanowski, W.; Li, E.; Martinez-Martin, D.; McEwan, A.; Wang, R.; Motion, A.; Bedoya, A. C.; Huang, J.; Azizi, L.; Eggleton, B. J., Research Priorities for COVID-19 Sensor Technology. *Nat. Biotechnol.* **2021**, *39*, 144.

(42) Ates, H. C.; Yetisen, A. K.; Güder, F.; Dincer, C. Wearable Devices for the Detection of COVID-19. *Nature Electronics* **2021**, *4* (1), 13−14.

(43) Broughton, J. P.; Deng, X.; Yu, G.; Fasching, C. L.; Servellita, V.; Singh, J.; Miao, X.; Streithorst, J. A.; Granados, A.; SotomayorGonzalez, A.; Zorn, K.; Gopez, A.; Hsu, E.; Gu, W.; Miller, S.; Pan, C.-Y.; Guevara, H.; Wadford, D. A.; Chen, J. S.; Chiu, C. Y. CRISPR−Cas12-Based Detection of SARS-CoV-2. *Nat. Biotechnol.* **2020**, *38* (7), 870−874.

(44) Dao Thi, V. L.; Herbst, K.; Boerner, K.; Meurer, M.; Kremer, L. P.; Kirrmaier, D.; Freistaedter, A.; Papagiannidis, D.; Galmozzi, C.; Stanifer, M. L.; Boulant, S.; Klein, S.; Chlanda, P.; Khalid, D.; Barreto Miranda, I.; Schnitzler, P.; Kräusslich, H.-G.; Knop, M.; Anders, S. A Colorimetric RT-Lamp Assay and Lamp-Sequencing For Detecting SARS-CoV-2 RNA in Clinical Samples. *Sci. Transl. Med.* **2020**, *12* (556), No. eabc7075.

(45) Flynn, M. J.; Snitser, O.; Flynn, J.; Green, S.; Yelin, I.; Szwarcwort-Cohen, M.; Kishony, R.; Elowitz, M. B. A Simple Direct RT-Lamp SARS-CoV-2 Saliva Diagnostic. *medRxiv* **2021**, DOI: 10.1101/2020.11.19.20234948.

(46) Subsoontorn, P.; Lohitnavy, M.; Kongkaew, C. The Diagnostic Accuracy of Isothermal Nucleic Acid Point-Of-Care Tests For Human Coronaviruses: A Systematic Review and Meta-Analysis. *Sci. Rep.* **2020**, *10* (1), 22349.

(47) Salazar-Vazquez, J.; Mendez-Vazquez, A. A Plug-And-Play Hyperspectral Imaging Sensor Using Low-Cost Equipment. *HardwareX* **2020**, *7*, No. e00087.

(48) Wu, D.; Sun, D.-W. Advanced Applications of Hyperspectral Imaging Technology For Food Quality and Safety Analysis and Assessment: A Review — Part II: Applications. *Innovative Food Sci. Emerging Technol.* **2013**, *19*, 15−28.

(49) Carrell, C.; Kava, A.; Nguyen, M.; Menger, R.; Munshi, Z.; Call, Z.; Nussbaum, M.; Henry, C. Beyond the Lateral Flow Assay: A Review of Paper-Based Microfluidics. *Microelectron. Eng.* **2019**, *206*, 45−54.

(50) Reboud, J.; Xu, G.; Garrett, A.; Adriko, M.; Yang, Z.; Tukahebwa, E. M.; Rowell, C.; Cooper, J. M. Paper-Based Microfluidics for DNA Diagnostics of Malaria In Low Resource Underserved Rural Communities. *Proc. Natl. Acad. Sci. U. S. A.* **2019**, *116* (11), 4834−4842.

(51) Fu, H.; Song, P.; Wu, Q.; Zhao, C.; Pan, P.; Li, X.; Li-Jessen, N. Y. K.; Liu, X. A Paper-Based Microfluidic Platform with Shape-Memory-Polymer-Actuated Fluid Valves For Automated Multi-Step Immunoassays. *Microsystems & Nanoengineering* **2019**, *5* (1), 50.

(52) Qiao, B.; Olvera de la Cruz, M. Enhanced Binding of SARS-CoV-2 Spike Protein to Receptor by Distal Polybasic Cleavage Sites. *ACS Nano* **2020**, *14* (8), 10616−10623.

(53) Andersen, K. G.; Rambaut, A.; Lipkin, W. I.; Holmes, E. C.; Garry, R. F. The Proximal Origin of SARS-CoV-2. *Nat. Med.* **2020**, *26* (4), 450−452.

(54) Gupta, A.; Madhavan, M. V.; Sehgal, K.; Nair, N.; Mahajan, S.; Sehrawat, T. S.; Bikdeli, B.; Ahluwalia, N.; Ausiello, J. C.; Wan, E. Y.; Freedberg, D. E.; Kirtane, A. J.; Parikh, S. H.; Maurer, M. S.; Nordvig, A. S.; Accili, D.; Bathon, J. M.; Mohan, S.; Bauer, K. A.; Leon, M. B. Extrapulmonary Manifestations of COVID-19. *Nat. Med.* **2020**, *26* (7), 1017−1032.

(55) Kordzadeh-Kermani, E.; Khalili, H.; Karimzadeh, I. Pathogenesis, Clinical Manifestations and Complications of Coronavirus Disease 2019 (COVID-19). *Future Microbiol.* **2020**, *15* (13), 1287−1305.

(56) Nishiga, M.; Wang, D. W.; Han, Y.; Lewis, D. B.; Wu, J. C. COVID-19 and Cardiovascular Disease: From Basic Mechanisms to Clinical Perspectives. *Nat. Rev. Cardiol.* **2020**, *17* (9), 543−558.

(57) Madjid, M.; Safavi-Naeini, P.; Solomon, S. D.; Vardeny, O. Potential Effects Of Coronaviruses on the Cardiovascular System: A Review. *JAMA Cardiology* **2020**, *5* (7), 831−840.

(58) Paramasivam, A.; Priyadharsini, J. V.; Raghunandhakumar, S.; Elumalai, P. A Novel COVID-19 and Its Effects on Cardiovascular Disease. *Hypertens. Res.* **2020**, *43* (7), 729−730.

(59) Jia, X.; Xiao, L.; Liu, Y., False Negative RT-PCR and False Positive Antibody Tests−Concern and Solutions in the Diagnosis of COVID-19. *J. Infect.* **2021**, *82*, 414.

(60) Wölfel, R.; Corman, V. M.; Guggemos, W.; Seilmaier, M.; Zange, S.; Müller, M. A.; Niemeyer, D.; Jones, T. C.; Vollmar, P.; Rothe, C.; Hoelscher, M.; Bleicker, T.; Brünink, S.; Schneider, J.; Ehmann, R.; Zwirglmaier, K.; Drosten, C.; Wendtner, C. Virological Assessment of Hospitalized Patients with COVID-2019. *Nature* **2020**, *581* (7809), 465−469.

(61) Brooks, Z. C.; Das, S. COVID-19 Testing: Impact of Prevalence, Sensitivity, and Specificity on Patient Risk And Cost. *Am. J. Clin. Pathol.* **2020**, *154* (5), 575−584.

(62) Mathuria, J. P.; Yadav, R.; Rajkumar. Laboratory Diagnosis of SARS-CoV-2 - A Review of Current Methods. *J. Infect Public Health* **2020**, *13* (7), 901−905.

(63) Ding, Y.; Chan, C. Y.; Lawrence, C. E. S-fold Web Server for Statistical Folding and Rational Design Of Nucleic Acids. *Nucleic Acids Res.* **2004**, *32*, W135−W141.

(64) Schmidt, M. W.; Baldridge, K. K.; Boatz, J. A.; Elbert, S. T.; Gordon, M. S.; Jensen, J. H.; Koseki, S.; Matsunaga, N.; Nguyen, K. A.; Su, S.; Windus, T. L.; Dupuis, M.; Montgomery, J. A., Jr General Atomic And Molecular Electronic Structure System. *J. Comput. Chem.* **1993**, *14* (11), 1347−1363.

(65) Morris, G. M.; Huey, R.; Lindstrom, W.; Sanner, M. F.; Belew, R. K.; Goodsell, D. S.; Olson, A. J. Autodock4 and Autodocktools4: Automated Docking with Selective Receptor Flexibility. *J. Comput. Chem.* **2009**, *30* (16), 2785−91.

(66) Moitra, P. A Combinatorial Approach Of Structure-Based Virtual Screening and Molecular Dynamics Simulation towards the Discovery Of A Highly Selective Inhibitor For VP9 Coat Protein of Banna Virus. *Bioorg. Chem.* **2019**, *86*, 15−27.

(67) Moitra, P.; Subramanian, Y.; Bhattacharya, S. Concentration Dependent Self-Assembly of TrK-NGF Receptor Derived Tripeptide: New Insights from Experiment and Computer Simulations. *J. Phys. Chem. B* **2017**, *121* (4), 815−824.